

TECHNISCHE
UNIVERSITÄT
DRESDEN

Study of Sensitive Variables for dim-8 EFT Operators in Same Charge WW jj Scattering

Bachelor-Arbeit
zur Erlangung des Hochschulgrades
Bachelor of Science
im Bachelor-Studiengang Physik

vorgelegt von

Pia Marie Müller
geboren am 16.04.1999 in Heidelberg

Institut für Kern und Teilchenphysik
Fakultät Physik
Bereich Mathematik und Naturwissenschaften
Technische Universität Dresden
2022

CERN-THESIS-2022-029
04/04/2022



Eingereicht am 30. März 2022

1. Gutachter: Dr. Frank Siegert
2. Gutachter: Prof. Dr. Arno Straessner

Summary

Abstract

English:

The weak vector boson scattering (VBS) at the Large Hadron Collider provides an excellent source of information on the structure of quartic gauge coupling and possible effects of physics beyond the Standard Model (SM) on electroweak symmetry breaking. By introducing Effective field theory (EFT) operators of higher mass dimension into a so called effective Lagrangian a wide variety of Beyond SM physics can be studied. For the scattering of two same sign W^\pm bosons the lowest important operators are of dimension 8. This thesis investigates the sensitivity of different variables to dim-8 EFT operators. Monte Carlo Simulations based on the Run 2 proton-proton collisions with VBS signature as input data are used. After identifying the most sensitive variables, a bin optimization algorithm is performed. Clipping, the recommended method for the unitarisation of Beyond Standard Model effects, is introduced and applied to different center-of-mass energies of the $W^\pm W^\pm$ -scattering. Using a fitting framework, limits on the coupling coefficients of the EFT operators are extracted. By comparing the limits to theoretical unitarity bounds, a range of validity with regards to unitarity is identified for the individual EFT operators.

Abstract

Deutsch:

Die Streuung von schwach geladenen Vektorbosonen (VBS) am Large Hadron Collider bietet Einblicke in die Struktur der Vierer-Kopplung und weiteren möglichen Effekten jenseits des Standardmodells (BSM). Durch die Einführung von Effektiven Feld Theorien (EFT) Operatoren in eine effektive Lagrangedichte können eine Vielzahl von BSM Effekten quantisiert werden. Diese Arbeit untersucht die Sensitivität verschiedener Variablen gegenüber dim-8 EFT Operatoren. Dafür werden Monte-Carlo-Simulationen, welche wiederum auf den RUN 2 Proton-Proton Kollisionen am LHC basieren, untersucht. Clipping, eine Methode für die Unitarisierung von Effekten jenseits des SM wird eingeführt und für verschiedene Schwerpunktsenergien der $W^\pm W^\pm$ Streuung angewendet. Nach der Durchführung eines Bin-Optimierungsalgorithmus folgt die weitere Auswertung in einem fitting Framework. Dieses ermöglicht die Ermittlung von statistischen Limits der Kopplungskoeffizienten für die EFT Operatoren. Für die einzelnen Operatoren wird ein Gültigkeitsbereich in Bezug zu Unitarität ermittelt.

Abbreviations

SM	Standard Model of Particle Physics
BSM	Beyond Standard Model
ssWW	same sign WW
EFT	Effective Field Theories
WIP	Work in Progress
LHC	Large Hadron Collider
ATLAS	A Toroidal LHC Apparatus
VBS	Vector Boson Scattering
CAF	Common Analysis Framework

Contents

1	Introduction	2
2	Experimental Setup	4
2.1	Large Hadron Collider	4
2.2	ATLAS Detector	5
3	Theoretical Foundations	7
3.1	Beyond Standard Model Research	7
3.2	Effective Field Theories	8
3.3	$W^\pm W^\pm$ scattering	11
3.4	Effective Field Theories and $W^\pm W^\pm$ Scattering	12
3.5	Unitarity Restrictions	14
4	Data Analysis Methods	16
4.1	Monte Carlo Simulations	16
4.2	Maximum Likelihood Method	16
5	Data Preparation	18
5.1	Kinematic Distributions and Sensitive Variables	18
5.2	Bin Optimization	22
6	Statistical Limits	25
6.1	Statistical limits for the Different Variables	25
6.2	Statistical Limits for Different Binnings	26
6.3	Clipping Scan	27
7	Summary and Outlook	30
8	Bibliography	33
9	Appendix	36

1 Introduction

The main objective of elementary particle physics is to understand the composition of the universe on the smallest possible scale. Many of the accomplishments in particle physics can be dated to the latter half of the 20th century. While theorists were concerned about the construction of a consistent theory, the experimental side developed experiments that became increasingly more complex to test the theoretical predictions. Their joint effort resulted in a so far unsurpassed theory, the Standard Model (SM) of Particle Physics. The SM consists of 4 types of force-carrying particles, the photon, gluon, W-boson and Z-boson, which are a direct consequence of the gauge symmetries of the SM. Additionally, 12 fundamental spin 1/2 particles make up the fundamental building blocks of matter. The latest addition to the SM is the Brout-Englert-Higgs-mechanism. The introduced Higgs-field ensures that the matter particles and the W and Z bosons retain their mass. The predictions of the SM were confirmed with great precision in set-ups like the Large Hadron Collider (LHC). The discovery of the Higgs boson at CERN in 2012 marks the end of the experimental search for particles predicted by the SM. But there is a downside to the success story of the SM. Some things, the SM just can't explain. It is, for example unable to explain the neutrino oscillations or the matter-antimatter antisymmetry in the universe. Another problem lies within the mathematical framework of the SM itself. It is not consistent with General Relativity, and only 3 of the 4 fundamental forces are included. This sets particle physics up with the new task to look beyond the known borders of the SM. While there are some theories which try to expand the SM, the experimental side of this proves to be challenging. Particle physics is already referred to as High Energy Physics. The research is performed in enormous particle colliders, which produce center-of-mass energies of up to 13 TeV. In order to find signs of beyond SM physics such as heavier particles, which are not yet included in the SM, the available energy regime needs to be expanded even further. The LHC is equipped with top of the art technology and any improvements on the total collision energy take years to implement. During this time, there are other ways to derive possible effects of higher energy physics in the currently available energy region. One of these are Effective Field Theories (EFT), which will be the main focus of this work. In chapter 2 and chapter 3 this work provides insights into the experimental and theoretical foundations of Beyond Standard Model Research. This includes an overview of the current experimental set-up and introducing a promising process for EFT studies, the $W^\pm W^\pm \rightarrow W^\pm W^\pm$ scattering. Next, chapter 4 presents the applied statistical

methods. The following chapter 5 and chapter 6 focus on preparing the data for the analysis and then studying the sensitivity of different variables to EFT operators as well as identifying a range of validity for each of the operators with regard to unitary restrictions. Lastly, chapter 7 presents an overview of the results and an outlook for subsequent research.

2 Experimental Setup

2.1 Large Hadron Collider

The Large Hadron Collider (LHC) [1] is the worlds largest circular particle accelerator and collider. Its main objective is to enable searches for new physics effects in a wide variety of potential scenarios. It was built built by the European Organization for Nuclear Research (CERN) between 1998 and 2008. The sheer size and many technological masterpieces allow high energy particle collisions which then can be analysed in four major experimental setups: ALICE, ATLAS, CMS and LHCb. The general build of the LHC can be comprehended using Figure 2.1. The main experiments take place as deep as 175 m below the surface. Before entering the LHC the particles (mainly protons but heavy ions are also possible) get accelerated in smaller setups such as the Super Proton Synchrotron (SPS). While entering the LHC the beam is split up into two beams travelling into opposite directions. The LHC then speeds up the particles even further with a current record of 6.5 TeV per beam. The beams travel in separate ultra high vacuum pipes which only intersect at the experiments. This results in a total collision energy of 13 TeV.

The particle rate $\frac{dN}{dt}$ of a given process at the intersection points can be calculated by:

$$\frac{dN}{dt} = \sigma \cdot \mathcal{L} \quad (2.1)$$

Where σ is the cross section, a measure of the probability that the specific process will take place, and the luminosity \mathcal{L} which is defined as followed:

$$\mathcal{L} = \frac{N_b f n_b}{4\pi\sigma_x\sigma_y} \cdot F \quad (2.2)$$

Here N_b is the number of protons per bunch, f the revolution frequency, n_b the number of bunches, $\sigma_{x,y}$ the beam width in x- and y-direction for a gaussian beam profile and lastly F represents any geometric corrections for the real beam shape. At the end of 2018, a luminosity of nearly $140 \frac{1}{\text{fb}}$ was recorded.

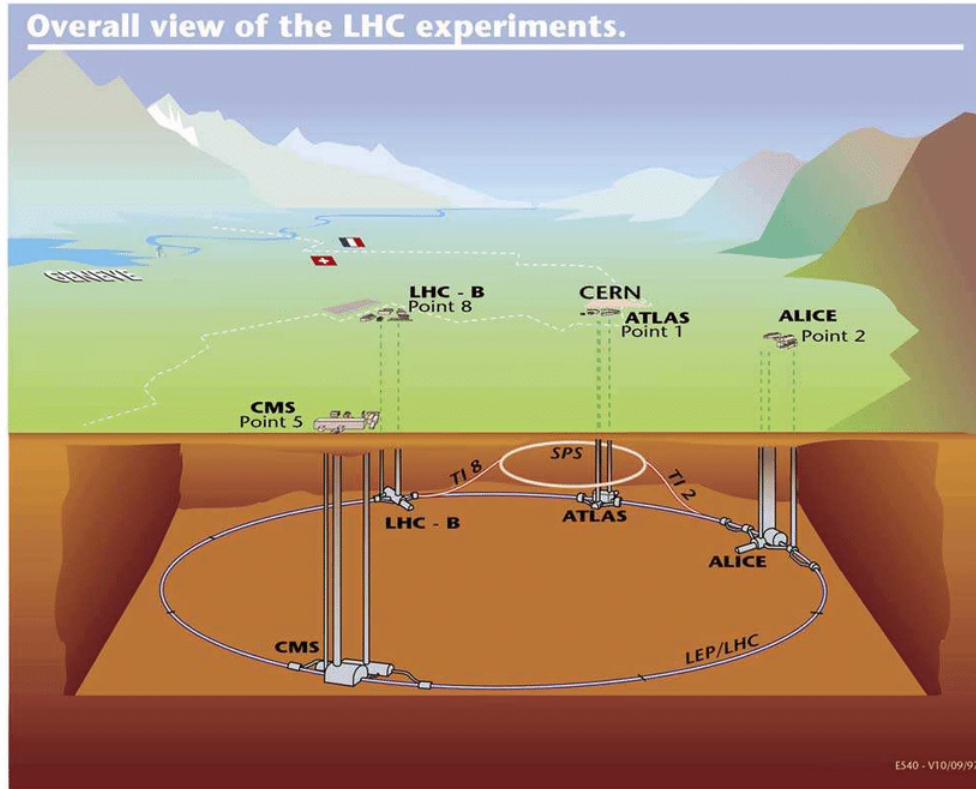


Figure 2.1: Schematic build of the LHC including the four major experiments ALICE, ATLAS, CMS and LHCb. Its circumference spans roughly 27 km.

2.2 ATLAS Detector

The experimental work of ATLAS¹ is mainly focused on precision measurements. It is built to identify outgoing particles and reconstructing underlying kinematics. As seen in Figure 2.2 the detector is built forward-backwards symmetric in regards to the collision points. It is installed in concentric layers around the beam pipe. Each layer has its own purpose in order to guarantee successful measurements.

Inner Detector The innermost layer traces the trajectories of charged particles. These trajectories can be used to measure the transverse momentum p_T of these particles. By installing a magnetic system parallel to the beam axis, the particle traces are bend in the transverse plane with a curvature of radius r_T depending on their charge q . Using the equation for the Lorentz force:

$$p_T = |q|Br_T \quad (2.3)$$

Calorimeter Calorimeters are used to measure the energy of electrically and strongly charged particles. The Calorimeter itself consists of an electromagnetic and a hydronic calorimeter.

¹A Toroidal LHC ApparatuS [2]

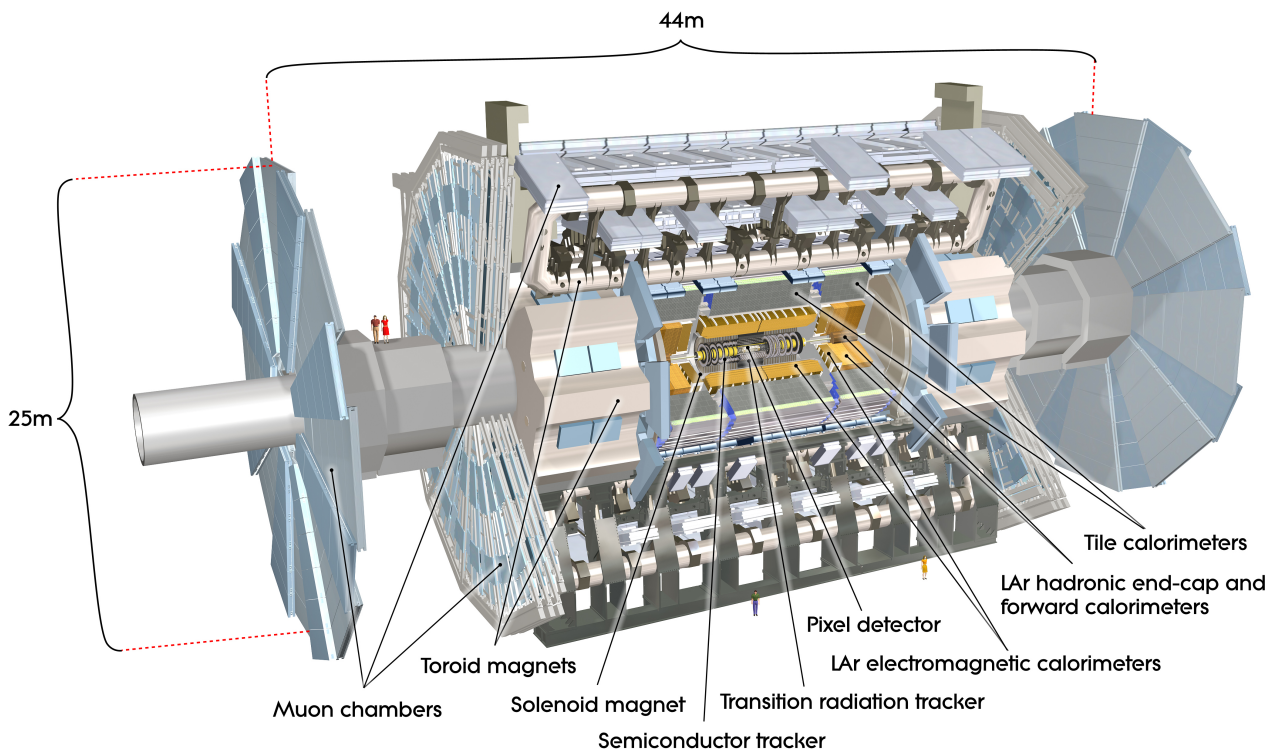


Figure 2.2: Built of the ATLAS Detector (quelle.) The detector is built in a cylindrical installation of concentric layers around the beam pipe. Graphic taken from [3]

Electrons and photons will leave their energy in the electromagnetic calorimeter by forming electromagnetic particle showers. These showers help to identify the particles. Hadrons, on the other hand, are typically heavier. Their corresponding shower process, the hadronic shower, starts later in the Hadronic Calorimeter. Again, leaving traces which can be used to measure their energy.

Muon Spectrometer Mouns are roughly 200 times heavier than electrons. They're able to pass both of the calorimeters without giving all their energy to the detector. Analogous to the Inner Detector, the outer most layer trace the trajectories of the surpassing particles.

3 Theoretical Foundations

3.1 Beyond Standard Model Research

The strong collaboration between theorists and experimentalists resulted in the SM as it is known today. Yet the research community has little doubt that the SM is not the end of the story. There are plenty of hints that lead to suspect there is more to come. The SM for example, is unable to unify all four fundamental forces into a consistent theory. While the strong, weak and electromagnetic force are part of the SM, gravity is described by its own theory, the theory of General Relativity. Further, there is no scientific consensus on why the weak force is 10^{24} times stronger than gravity. This problem is referred to as the hierarchy problem. There are also some fine-tuning problems to the SM such as the charge-parity problem or the insufficient explanation of the matter-antimatter asymmetry in the universe.

In the last century, theorists have set up different theories, which then needed to be confirmed or refuted by experimentalists. The cross section σ for different processes served as a bridge between theory and experiment, since it could be determined either way. So far, this has been done using a direct approach. Particle colliders such as the LHC were able to generate high enough invariant masses to directly detect new particles via resonances in cross sections. The latest example is the discovery of the Higgs boson, which was predicted by Peter Higgs in the 1960s. In 2012 the LHC was able to produce center-of-mass energy so that the mass of the Higgs-boson could be reconstructed from the decay products of proton-proton collisions. At the given point in time, particle colliders, which offer much higher invariant masses, are not accessible. Due to technical obstacles, even a small increase is challenging. The indirect approach offers an alternative method to look for hints of beyond SM physics. It is more focused on the tails of kinematic distributions, where small deviations from SM predictions could deliver meaningful inference of higher energy physics. The comparison between the two approaches is visualised in Figure 3.1.

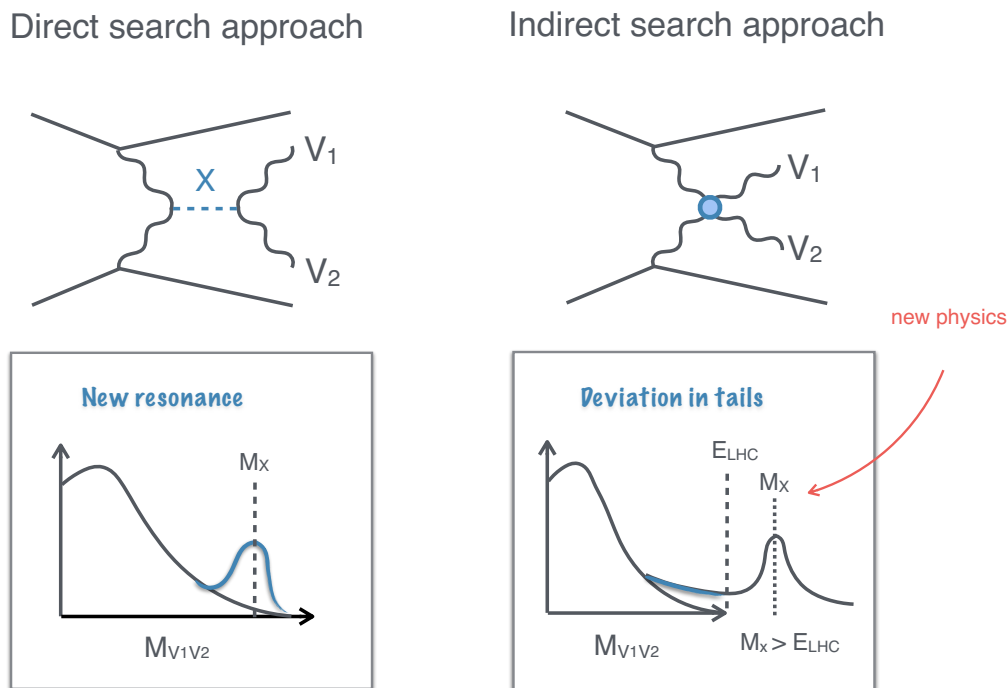


Figure 3.1: Comparison between the direct and indirect approach to discover new particles. In the direct approach, the particle’s mass M_x is within the energy range E_{LHC} of current experimental setups such as the LHC. The presence of a new particle can be directly derived from the bump in the kinematic distribution. In the indirect approach, the resonance falls above the available energy. Yet the peak evokes small deviations in the tail of the kinematic distribution which (using the right setup) might be variable. Illustration taken from [4].

3.2 Effective Field Theories

Effective field theories offer a framework to quantify these variations. [5], [6] and [7] present nice, in depth introductions into the topic. In general, a theory is labelled as effective if it successfully describes a physical scenario at a restricted validity range (e.g. low energies or large distances). On top of that, SM EFT are consistent with quantum field theory and the symmetries of the SM. Namely $SU(3)_C \times SU(2)_L \times U(1)_Y$ and Lorentz invariance. Its purpose is to describe the effects of a variety of different beyond Standard Model effects. This means that the framework is so general that new physics could come from a wide variety of different causes. This is useful in two respects: On one hand, the search for new physics can be executed without committing to a particular extension of the SM. On the other hand, if no new physics is discovered, the accuracy with which new physics is excluded can be quantified. Still, there are some physical assumptions which each effective field theory should fulfil:

-
- I No new light degrees of freedom (e.g. light particles) are added, since there is no experimental backup to justify this.
 - II Dynamics at low energies do not depend on details of dynamics at high energies.
 - III Non-local heavy particle exchanges are replaced by a tower of local (non-renormalizable) interactions among light particles.
 - IV There is a Higgs-doublet with linear representation and the heavy degrees of freedom do not mix with the Higgs-doublet. The theory stays renormalizable after removing them.

Generally, there are two different approaches to effective field theories:

top-down approach The underlying theory is known, but the EFT is easier to use (e.g. less computational work) while not compromising too much on accuracy.

bottom-up approach The full theory is not known yet and by considering EFT one might get insight into what the full theory should contain. One prominent example of a bottom-up approach is the Fermi Theory of beta decay, which can be seen as a precursor of the electroweak theory. Fermi made up this theory in order to explain beta decay without any knowledge of the existence of the W boson. His theory however, was only able to withstand at lower energies, failing to predict correct cross sections when the center-of-mass energy approaches the mass of the W boson. It is important to note that Fermi at the time was not keen about developing an EFT but he was rather searching for a full theory. Now that the electroweak theory is known, Fermi's theory was not discarded but rather used in a top-down manner to make the calculations of matrix elements for low energy processes, such as weak hadron decays, easier.

Since the current goal is to broaden knowledge of higher energy physics, the bottom-up approach is the way to go. This is done by expanding the SM-Lagrangian by operators of higher mass dimensions. These operators quantify new, short-distance interactions. Assuming that the scale of new physics Λ is large in comparison to the electroweak scale, a SMEFT-Lagrangian can be written as:

$$\mathcal{L}_{EFF} = \mathcal{L}_{SM} + \frac{a_5}{\Lambda} \mathcal{O}^{(5)} + \sum_i \frac{a_i}{\Lambda^2} \mathcal{O}^{(6)} + \sum_i \frac{a_i}{\Lambda^4} \mathcal{O}^{(8)} + \dots \quad (3.1)$$

Where a_i are dimensionless coefficients, which parameterize the strength of the coupling to SM particles, Λ is the (energy-) scale of new physics and \mathcal{O}_i are the EFT operators of higher mass dimension. Further, a summarising coefficient $f_i^n = \frac{a_i}{\Lambda^n}$, the Wilson coefficient, is introduced. The construction of these higher dimensional operators will be discussed in section 3.4.

One analogy which allows for a more intuitive understanding is the concept of Taylor expansions. Taking for example, the function $f(x) = \sin(x)$. This functions Taylor expansion

$$T_{f(x,0)} = x - \frac{1}{3!}x^3 + \frac{1}{5!}x^5 - \frac{1}{7!}x^7 \dots \quad (3.2)$$

resembles the idea behind the effective Lagrangian. Each tries to approximate their initial form. Starting with a leading order term x or \mathcal{L}_{EFF} , which is able to match the reality for small x in case of $T_{f(x,0)}$ or low energies in case of \mathcal{L}_{EFF} . As seen in Figure 3.2 by adding higher order terms the deviations between reality and expansion can be minimised.

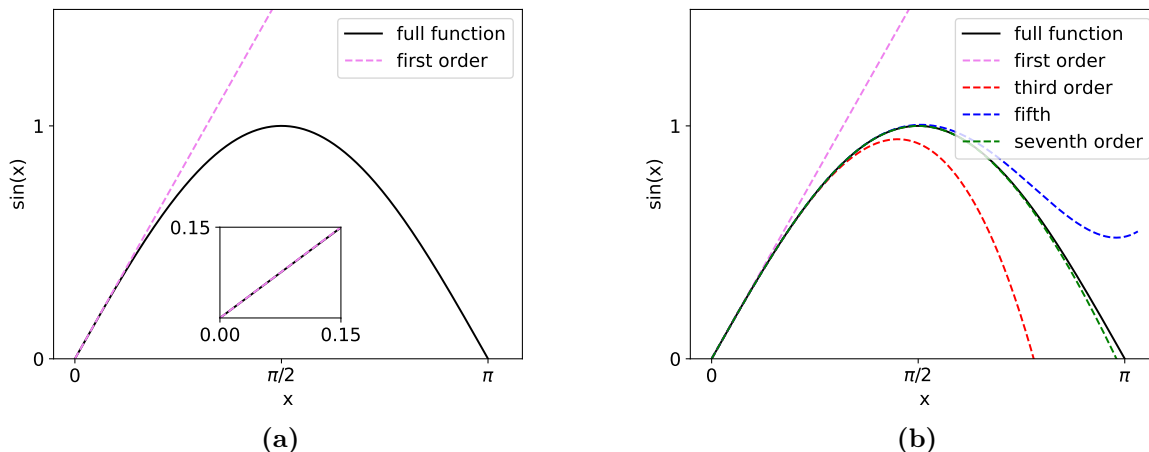


Figure 3.2: Analogy for Taylor expansions and effective Lagrangian's for the function $f(x) = \sin(x)$. In subplot (a) the first order Taylor expansion (SM) and the full function (nature) is shown. For small x (low energies) the expansion of first order presents a good approximation. If the observation range is close enough to the development point, the deviations become unnoticeable (smaller subplot). But it becomes clear that for bigger values of x the first order fails to align with the full function. By adding more orders (EFT operators) to the expansion in subplot (b) the deviations can be minimised up to a certain value of x .

3.3 $W^\pm W^\pm$ scattering

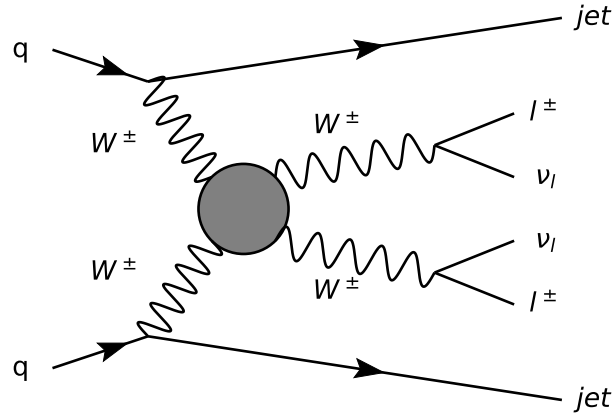


Figure 3.3: $W^\pm W^\pm$ scattering as part of a proton-proton collision.

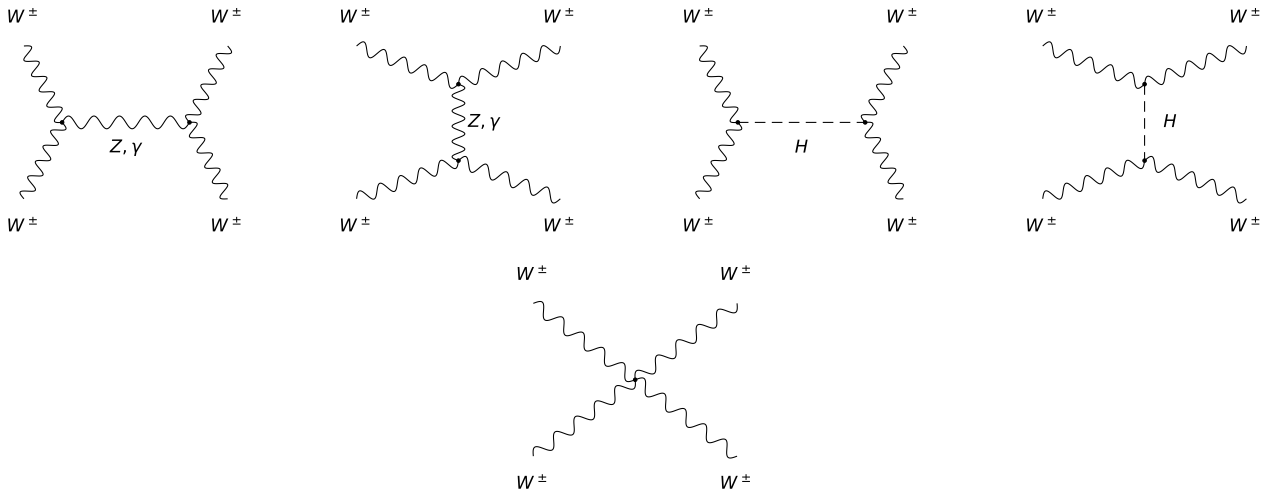


Figure 3.4: All leading-order Feynman diagrams that connect two initial W^\pm and two final W^\pm . If the Higgs-boson was not included, the cross section for this process would violate unitarity. Therefore all diagrams are needed in order to construct the full theory. The first three diagrams derive from the gauge structure of the SM while the last two are directly related to the electroweak-symmetry breaking.

There is currently no experimental setup to solely measure vector boson scattering. Luckily the same sign WW (ssWW) scattering is a sub-process of proton proton collision

$$pp \rightarrow W^\pm W^\pm + 2jets \rightarrow l^\pm \nu l^\pm \nu + 2jets \quad (3.3)$$

and therefore data from the LHC can be used for research. The process can be seen in 3.3. Protons are not elementary particles themselves. They consist of two up and one down quark. For the ssWW scattering, two of the quarks emit a W^\pm -boson. The circle sums up all possible vertices for vector boson scattering. It is broken down further in Figure 3.4. The two bosons

decay into two same charged leptons and their associated neutrinos. Meanwhile, hadronization of the quarks then leads to the formation of jets, which together with the two leptons will be the main detectable decay products in the LHC.

The ssWW process is only one of many possible sub-processes of the proton-proton collision. For that reason it is necessary to separate the other processes from those with ssWW signature. This is done by implementing special selection criterias into the analysis framework. [8] offers a detailed descriptions on the criterias listed in Table 3.1.

Exactly two Tight leptons with identical electrical charge
No Veto leptons
Electrons pass the charge flip rejection
ee-channel: $ \eta < 1.37$, $ m_{ee} - m_Z > 15\text{GeV}$
$m_W > 20\text{GeV}$
$E_T^{miss} > 30\text{GeV}$
At least two jets
Leading jet: $p_T > 65\text{GeV}$
Subleading jet: $p_T > 35\text{GeV}$
b-jet veto
$ \Delta y_{jj} > 2$
$m_{jj} > 500\text{GeV}$

Table 3.1: Event selection for the signal region of the electroweak same charged W^\pm scattering.

3.4 Effective Field Theories and $W^\pm W^\pm$ Scattering

The interaction of two vector bosons is called vector bosons scattering (VBS). The process itself is extremely rare. Only now, with the gathered data from RUN 2 extensive VBS research became possible. There are a couple of reasons why the ssWW scattering or more general VBS is interesting for beyond SM research. Firstly, the weak interaction, which plays the main role in this process, is neatly described compared to quantum chromodynamics (QCD) processes, which require lots of approximations. This way, the VBS can be used for precision testing of the gauge structure of the SM. Secondly, as shown in Figure 3.4 the $W^\pm W^\pm \rightarrow W^\pm W^\pm$ scattering is directly related to Higgs-boson interaction. VBS measurements are regarded as complementary research to other Higgs-boson measurements at the LHC in order to investigate the bosons properties.

In order to describe the quartic interaction in terms of EFT expansions (see Equation 3.1) only parity conserving effective Lagrangian's are considered. Each of these higher dimensional operators can be contracted using few building blocks. Denoting by Φ , the Higgs doublet and

by U , an arbitrary $SU(2)_L$ transformation, these blocks are as followed [9]:

$$\Phi \rightarrow \Phi' = U\Phi \quad (3.4)$$

$$D_\mu\Phi \rightarrow D'_\mu\Phi' = UD_\mu\Phi \quad (3.5)$$

$$\hat{W}_{\mu\nu} = \sum iW_{\mu\nu}^j \frac{\sigma^j}{2} \rightarrow \hat{W}'_{\mu\nu} = U\hat{W}_{\mu\nu}U^\dagger \quad (3.6)$$

$$B_{\mu\nu} \rightarrow B'_{\mu\nu} = B_{\mu\nu} \quad (3.7)$$

Where $W_{\mu\nu}^j$ is the $SU(2)_L$ field strength and $B_{\mu\nu}$ is the $U(1)_Y$ one. The covariant derivative is given by

$$D_\mu\Phi = \left(\delta_\mu - igW_\mu^j \frac{\sigma^j}{2} - ig'B_\mu \frac{1}{2}\right)\Phi. \quad (3.8)$$

The lowest dimension of operators which result in quartic coupling and do not show two or three weak boson interactions are of dimension 8. Following the notation from [9] there are three different classes of operators. In total these classes contain 18 different operators. Yet, not all of them affect the ssWW scattering which is of interest in this thesis. A list of all deciding operators follows. A complete list can be found in [9].

Operators containing just $D_\mu\Phi$:

$$\begin{aligned} \mathcal{L}_{S,0} &= \left[(D_\mu\Phi)^\dagger D_\nu\Phi\right] \times \left[(D^\mu\Phi)^\dagger D^\nu\Phi\right] \\ \mathcal{L}_{S,1} &= \left[(D_\mu\Phi)^\dagger D^\mu\Phi\right] \times \left[(D_\nu\Phi)^\dagger D^\nu\Phi\right] \end{aligned} \quad (3.9)$$

Operators containing $D_\mu\Phi$ and field strength:

$$\begin{aligned} \mathcal{L}_{M,0} &= \text{Tr} \left[\hat{W}_{\mu\nu} \hat{W}^{\mu\nu} \right] \times \left[(D_\beta\Phi)^\dagger D^\beta\Phi \right] \\ \mathcal{L}_{M,1} &= \text{Tr} \left[\hat{W}_{\mu\nu} \hat{W}^{\nu\beta} \right] \times \left[(D_\beta\Phi)^\dagger D^\mu\Phi \right] \\ \mathcal{L}_{M,7} &= \left[(D_\mu\Phi)^\dagger \hat{W}_{\beta\nu} \hat{W}^{\beta\mu} D^\nu\Phi \right] \\ &+ \text{four non } W^\pm W^\pm \rightarrow W^\pm W^\pm \text{ affecting operators.} \end{aligned} \quad (3.10)$$

Operators containing just the field strength tensor:

$$\begin{aligned} \mathcal{L}_{T,0} &= \text{Tr} \left[\hat{W}_{\mu\nu} \hat{W}^{\mu\nu} \right] \times \text{Tr} \left[\hat{W}_{\alpha\beta} \hat{W}^{\alpha\beta} \right] \\ \mathcal{L}_{T,1} &= \text{Tr} \left[\hat{W}_{\alpha\nu} \hat{W}^{\mu\beta} \right] \times \text{Tr} \left[\hat{W}_{\mu\beta} \hat{W}^{\alpha\nu} \right] \\ \mathcal{L}_{T,2} &= \text{Tr} \left[\hat{W}_{\alpha\mu} \hat{W}^{\mu\beta} \right] \times \text{Tr} \left[\hat{W}_{\beta\nu} \hat{W}^{\nu\alpha} \right] \\ &+ \text{six non } W^\pm W^\pm \rightarrow W^\pm W^\pm \text{ affecting operators.} \end{aligned} \quad (3.11)$$

3.5 Unitarity Restrictions

Due to the additive structure of the EFT Lagrangian, the matrix element for a sub-process can be written as:

$$\left| A_{\text{SM}} + \sum_i \frac{c_i}{\Lambda^4} A_i \right|. \quad (3.12)$$

Where A_{SM} is the SM scattering amplitude and A_i refers to the contributions of the individual dimension 8 operators which have just been introduced. The squared matrix element which is then related to the cross section can be expressed by:

$$\left| A_{\text{SM}} + \sum_i \frac{c_i}{\Lambda^4} A_i \right|^2 = \underbrace{|A_{\text{SM}}|^2}_{\text{SM amplitude}} + \underbrace{\sum_i \frac{c_i}{\Lambda^4} 2 \text{Re}(A_{\text{SM}} A_i)}_{\text{interference term}} + \underbrace{\sum_i \frac{c_i}{\Lambda^8} |A_i|^2}_{\text{quadratic term}} + \underbrace{\sum_{ij, i \neq j} \frac{c_i c_j}{\Lambda^8} 2 \text{Re}(A_i A_j)}_{\text{interference term between operators}}. \quad (3.13)$$

The departure of the quartic interactions from the SM predictions will lead to the growth of the scattering amplitudes. At sufficiently high enough energies, any nonzero anomalous quartic couplings will violate unitarity. Noticeably, the cross section of the sub-process $W^\pm W^\pm \rightarrow W^\pm W^\pm$ will surpass the total proton-proton collision cross section. EFT are therefore not complete theories. In [10] the effort is made to obtain partial-wave unitarity constraints by assuming a linear realization of the $SU(2)_L \times U(1)_Y$ gauge symmetry. Two scenarios are considered: Firstly only one Wilson coefficient is non-vanishing and secondly all Wilson coefficients of a given operator subset are non-vanishing. The following results are stated in Table 3.2. An exemplary comparison for M7 between the two scenarios is shown in Figure 3.5

Wilson coefficient	1 operator	all operators of subset
$ f_{M0} $	$\frac{32}{\sqrt{6}}\pi s^{-2}$	$\frac{2}{3}(72 + 5\sqrt{6})\pi s^{-2}$
$ f_{M1} $	$\frac{128}{\sqrt{6}}\pi s^{-2}$	$8(24 + \frac{\sqrt{6}}{5})\pi s^{-2}$
$ f_{M7} $	$\frac{256}{\sqrt{6}}\pi s^{-2}$	$\frac{64}{5}(24 + \sqrt{6})\pi s^{-2}$
$ f_{S0} $	$32\pi s^{-2}$	$48\pi s^{-2}$
$ f_{S1} $	$\frac{96}{7}\pi s^{-2}$	$\frac{288}{5}\pi s^{-2}$
$ f_{T0} $	$\frac{12}{5}\pi s^{-2}$	$\frac{136}{11}\pi s^{-2}$
$ f_{T1} $	$\frac{24}{5}\pi s^{-2}$	$\frac{352}{31}\pi s^{-2}$
$ f_{T2} $	$\frac{24}{7}\pi s^{-2}$	$32\pi s^{-2}$

Table 3.2: Unitarity constrains on the Wilson coefficients for the operators relevant to sssWW scattering, when just one coefficient is non-vanishing (second column), as well as when all coefficients of the respective subset are included (third column). In the second scenario, the individual operators can not achieve their limits simultaneously since they are only extreme points in a multidimensional region spanned by all Wilson coefficients in the given subset.

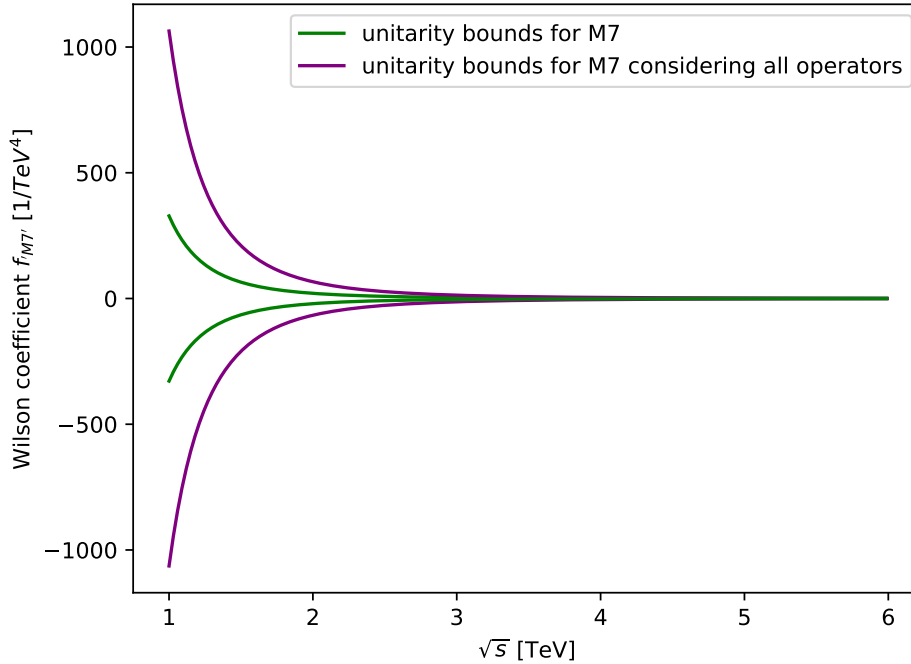


Figure 3.5: Comparison between unitarity constrains for one operator (green) and all operators of the M subset (purple). The purple line is much broader, since multiple operators are taken into consideration. The choice to present the boundaries over the center-of-mass energy \sqrt{s} instead of s will explain itself later, when a comparison with a quantity that depends on \sqrt{s} is drawn.

4 Data Analysis Methods

4.1 Monte Carlo Simulations

Data simulations are a key ingredient for the analysis of particle collisions. They are utilized to design analysis tools which later can be used on the final data. Simulations are also essential in order to compare theory predictions with experimental results. Instead of working with real data from LHC, this analysis uses Monte Carlo Simulations. These Simulations are complex in itself and only a brief introduction will be provided here since some of the vocabulary will be used in this thesis. For further detailed descriptions, see [7] [11]. To begin the simulations, the assumed theory must be specified. This could be the Standard Model or, as introduced earlier, additional EFT terms. The program then simulates the hard proton proton collision with all its sub-processes. This is called the truth level. Secondly, in order to be able to compare the simulated data to real data, the particle interactions with the detector need to be simulated as well. Afterwards, the same methods as for real data are used to identify the particles from the given detector entries. This level is called reconstruction level.

4.2 Maximum Likelihood Method

In most cases only a sample of a population is available for research. For further statistical analysis, being able to draw conclusions about important parameters from those samples is essential. The Maximum Likelihood Method is a general procedure in order to estimate parameters of an assumed probability distribution given some observed data. ¹

Given n individual measurements x_1, x_2, \dots, x_n and assuming a probability density function $f(x, a)$. f is characterized by a specific parameter a . (For a gaussian this parameter, eg. could be the mean value μ or the standard deviation σ). For infinitesimal small dx_i the probability to find the value x_i in the interval $[x_i, x_i + dx_i]$ is given by $f(x_i, a) \cdot [x_i, x_i + dx_i]$. Therefore the full probability of the n measurements is expressed by:

$$P = f(x_1, a) \cdot [x_1, x_1 + dx_1] \dots f(x_n, a) \cdot [x_n, x_n + dx_n] \quad (4.1)$$

Since the intervals are not depended on a a simplified expression, the **likelihood-function**

¹A more in depth guide on statistical methods in experimental physics can be found in [12].

$$\mathcal{L} = f(x_1, a) \cdot f(x_2, a) \cdot \dots \cdot f(x_n, a), \quad (4.2)$$

is sufficient. The best fit \hat{a} describes the parameter value which maximises the probability to receive the given sample from the assumed probability distribution. It is obtained by maximising the likelihood function \mathcal{L} :

$$\left. \frac{\delta \mathcal{L}}{\delta a} \right|_{a=\hat{a}} = 0 \quad (4.3)$$

For practical reasons it is often simpler to use the negative logarithmic likelihood-function

$$F(a) = -2 \ln \mathcal{L} = -2 \sum_{i=1}^n \ln(f(x_i, a)) \quad (4.4)$$

Since the logarithm is a monoton function, the minimum of $F(a)$ instead of the maximum can be determined in order to find the best fit value. This representation has one main advantage: If a gaussian distribution is assumed, the one and two σ environments can be determined easily. The one sigma environment is located where $F(a) - F(\hat{a}) = 1$ while for the two σ environment it is $F(a) - F(\hat{a}) = 4$.

5 Data Preparation

The following part of this thesis can be divided into three parts. Firstly, introducing the studied variables and discussing their sensitivity. Secondly, data preparation using the Common Analysis Framework (CAF [13]). This includes applying a bin optimization algorithm to the created histograms and introducing a technique referred to as clipping. Lastly, this output is transferred into a fitting framework to receive limits on the Wilson coefficients for each operator.

5.1 Kinematic Distributions and Sensitive Variables

All histogram in this thesis display the number of events over a given reconstruction level variable. In order to prove useful for BSM research a variable needs to

I show discriminant behaviour between EFT and SM ssWW events and/ or

II set the EFT events apart from the SM background.

A variable which fulfills one or both of these criteria is classified as sensitive. Following a previous work [14] this thesis mainly focuses on five variables which presented themselves as sensitive. The results of the previous work have been verified during this study. However, a detailed description will not be given since this study is more focused on building on top of these results. In the following part the variables will be introduced stating in square brackets $[\cdot]$, which criteria are fulfilled by this variable.

Mass reconstruction variables: Resonances in invariant mass distributions indicate a new particle. But due to the inability of the LHC to measure neutrinos, it is not possible to reconstruct the full invariant mass for the ssWW-scattering. Instead, different mass reconstruction variables are used. The following variables are so called mass-bound variables, this means that by construction their values are expected to be lower than the full WW invariant mass.

m_{ll} [I + II]: The invariant mass of the two leptons is calculated by the momentum of the two same charged leptons and the scattering angle $\cos(\Delta\theta(l_1, l_2))$:

$$m_{ll} = \sqrt{|\vec{p}_{l_1}| |\vec{p}_{l_2}| (1 - \cos(\Delta\theta(l_1, l_2)))}. \quad (5.1)$$

It is well defined and can be measured with high accuracy, yet it completely neglects any contributions from neutrinos. Next are the transverse projections. The detector setup makes it possible to reconstruct the missing energy E_T in the plane perpendicular to the beam axis (transverse plane). Depending on the calculation method, one can receive different transverse invariant masses (for more see [15], [16]):

m_{o1} [I + II]: The early-projected "mass less" invariant mass doesn't incorporate the masses of the leptons to begin with. It is calculated by:

$$m_{o1} = \sqrt{(|\vec{p}_{l_1T}| + |\vec{p}_{l_2T}| + E_T^{miss})^2 - (p_{1T} + \vec{E}_T^{miss})^2}. \quad (5.2)$$

With $\vec{p}_{1T} = \vec{p}_{l_1T} + \vec{p}_{l_2T}$.

m_T [I + II]: The late-projected "mass-preserving" invariant mass can be obtained by:

$$m_T = \sqrt{(\sqrt{m_{ll}^2 + \vec{p}_{1T}^2} + E_T^{miss})^2 - (\vec{p}_{1T} + \vec{E}_T^{miss})^2}. \quad (5.3)$$

Where m_{ll} is the invariant mass of the two leptons, which still incorporates the visible longitudinal momenta and \vec{p}_{1T} is defined as above.

Others:

R_{pt} [I + II]: Ratio between the products of the transverse momentum of the two leptons against the product of the transverse momentum of the two jets. It is calculated by:

$$R_{Pt} = \frac{p_T^{l_1} p_T^{l_2}}{p_T^{j_1} p_T^{j_2}}. \quad (5.4)$$

$\Delta\phi_{jets}$ [I]: Azimuthal angle between the two jets. This variable is included because it has shown great sensitivity for dijet production in association with the Z boson in [17].

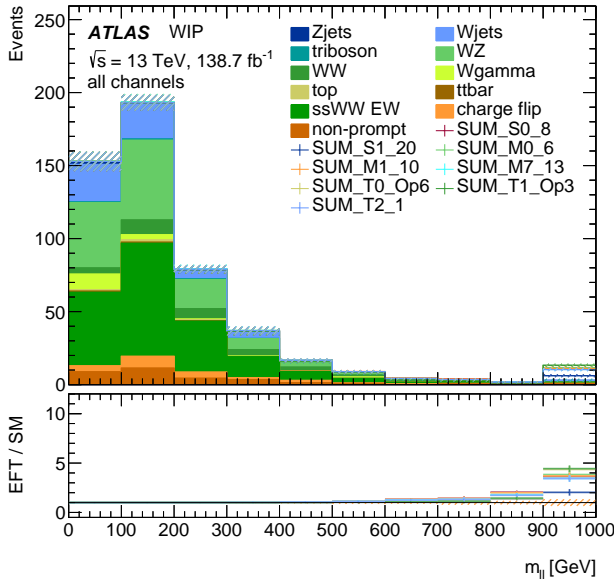
$\cos(\Delta\Phi_{leps})$ [I]: Cosine of the azimuthal angle between the two leptons l_1, l_2 .

All histograms in this thesis are created using CAF. For the ssWW-scattering, the resulting kinematic distribution can be seen in Figure 5.1. They are based on Run 2 measurements of 138.7 fb^{-1} collected by the ATLAS experiment at the LHC. The histograms contain SM background, ssWW scattering and EFT events. For display, each operator has an assigned coefficient c_n/Λ to quantify the coupling to the SM. An overview can be found in Table 5.1. Therefore the label M1_10 refers to the operator M1 with the specific coupling strength of

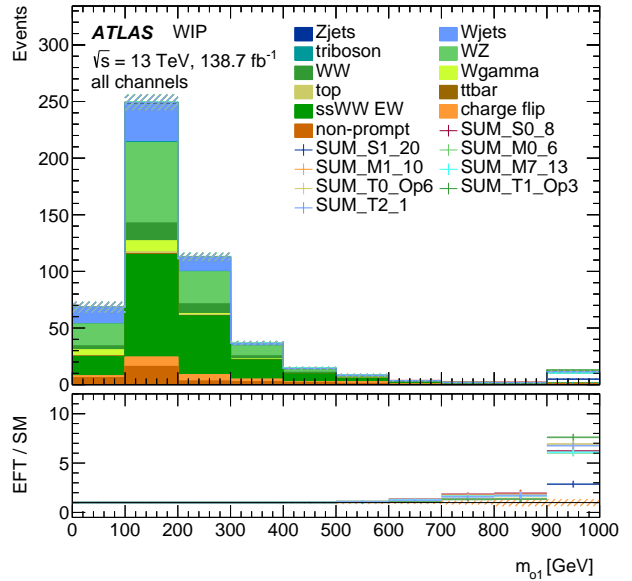
$10 \frac{1}{\text{TeV}^4}$. Apart from $\cos(\Delta\Phi_{leps})$ and $\Delta\phi_{jets}$, which have a strictly defined value range, the other histograms contain overflow bins. This means, that the last bin contains all events above the depicted maximal value. To avoid strongly pronounced overflow bins, the domain of definition has been chosen to portray most of the events.

	S0	S1	M0	M1	M7	T0	T1	T2
a_i/Λ^4	8	20	6	10	13	0.6	0.3	1

Table 5.1: Fixed coefficients for all EFT operators with $[c_n/\Lambda^4] = 1/\text{TeV}^{-4}$



(a) Kinematic distribution for m_{ll} .



(b) Kinematic distribution for m_{o1} .

As expected, the three variables m_{ll} , m_{o1} , m_T share similar behaviour. First a peak in SM events for relatively low energies and then an increase in EFT events for the higher energy regime. R_{tp} only shows one prominent bin at a low ratio, but compared to the other variables it presents the highest ratio between EFT and SM events. For $\Delta\phi_{jets}$ and $\cos(\Delta\Phi_{leps})$ it is not possible to make out an area where the EFT events discriminate against the SM predictions. The ratios remain comparably low for all values.

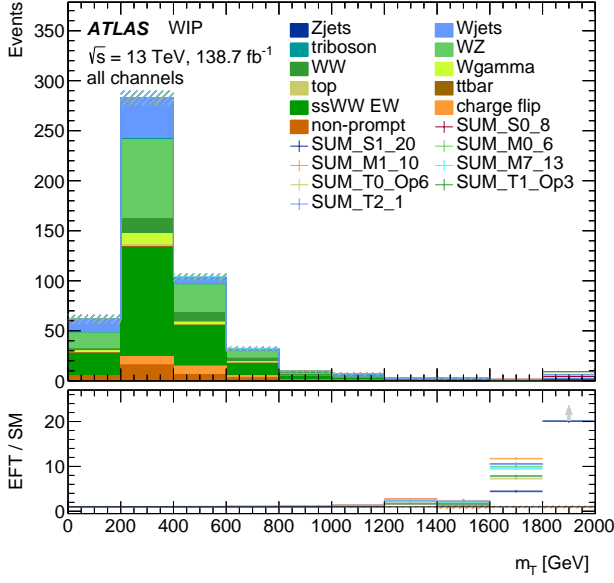
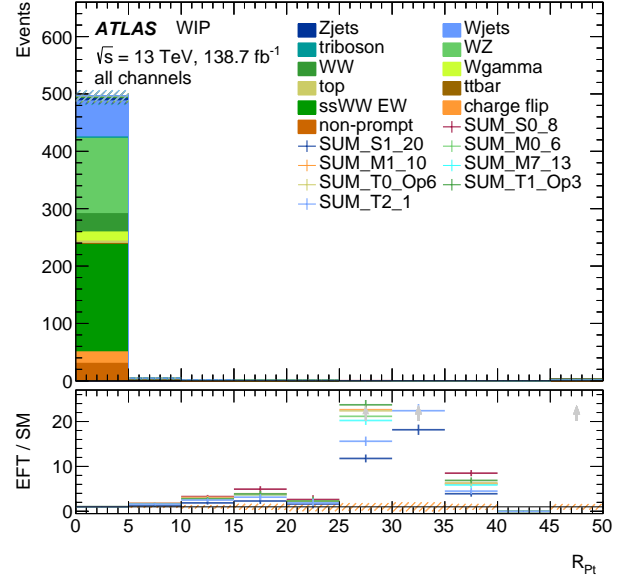
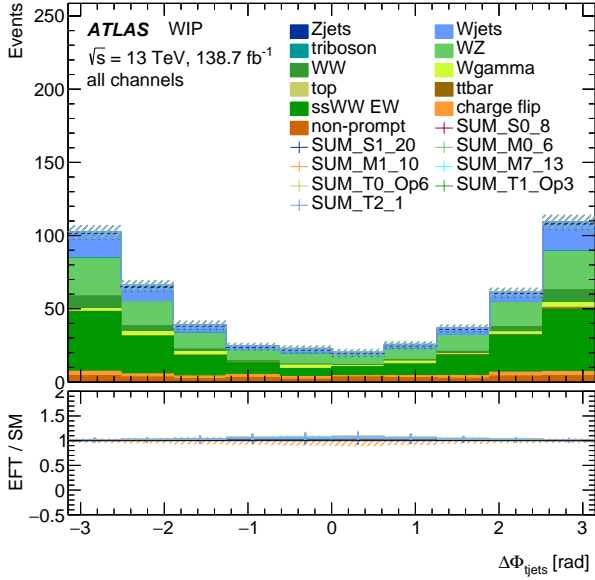
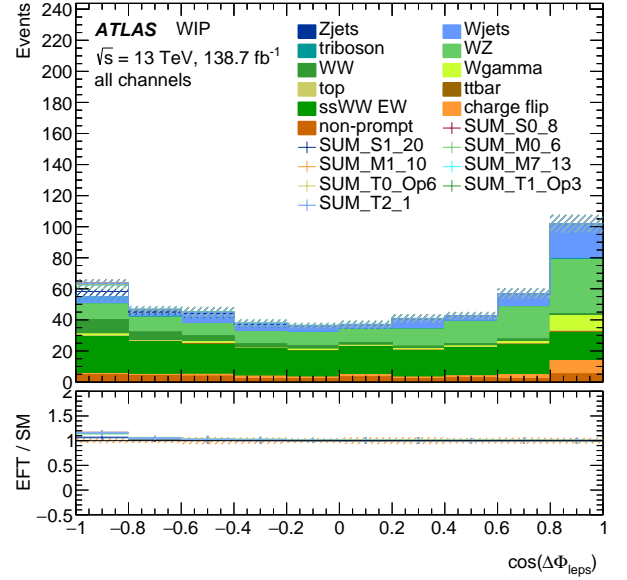
(c) Kinematic distribution for m_T .(d) Kinematic distribution for R_{Pt} .(e) Kinematic distribution for $\Delta\phi_{jets}$.(f) Kinematic distribution for $\cos(\Delta\phi_{leps})$.

Figure 5.1: Main plot: Kinematic distributions for each variable. The Standard Model predictions are stacked, while each EFT contribution is drawn as an individual line. The EFT events sum up both interference and quadratic terms. Subplot: Ratio between Standard Model predictions and the individual EFT operators and an additional reference line at zero.

To avoid many small contributions and since these processes are not of special interest in this study the Zjets, Wjets, top, non-prompt, Wgamma and ttbar events will be merged into one category called "Fakes" for further analysis.

5.2 Bin Optimization

Instead of using equidistant bin edges, a bin optimization algorithm is performed in order to fulfil the needs of further statistical analysis. The goal is to find a middle ground between not having too high statistical uncertainties and still guaranteeing an appropriate significance of the EFT events regarding the SM-background. The significance quantifies the probability of a statistical fluctuation to observe signal and backgrounds ($S + B$) events when only B is expected. A comparison between the significance and this probability is made in Table 5.2.

significance	1σ	2σ	3σ	4σ	5σ
probability	16%	2.3%	0.14%	$3 \cdot 10^{-5}\%$	$3 \cdot 10^{-7}\%$

Table 5.2: Significance of a signal [18] with the corresponding probability that the observation of the excess of events is due to a background statistical fluctuation.

In this chapter, only the bin optimization for m_{ll} will be comprehended. However, the procedure is analogous for the other variables. Starting with a relatively fine binning for each of the EFT operators (e.g. 100 bins as seen in Figure 5.2a) the algorithm then reduces the amount of bins following specific criteria.

In a first run, the algorithm scans all bins from right to left regarding two conditions:

Maximal Uncertainty: If the maximal uncertainty of an individual bin is over 0.3 the bin gets merged with one of its neighbours, depending on which merge results in the least significance decrease.

Minimal Events: If the bin contains fewer than 10 background events the bin gets merged with one of its neighbours.¹

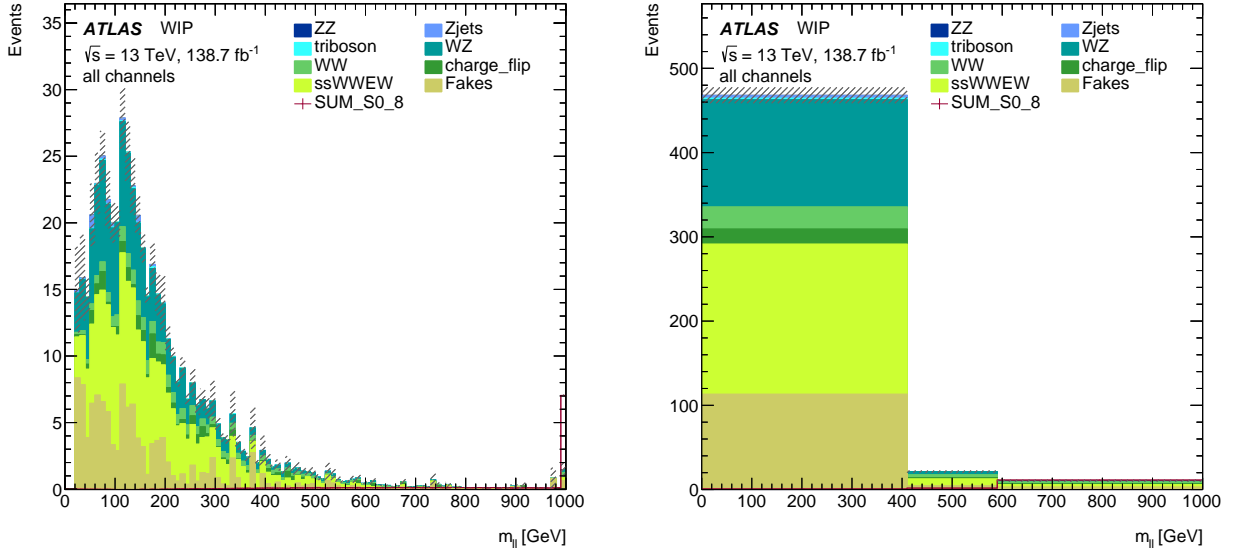
In a second run neighbouring bins are merged if the significance decrease falls below 3%.

Operator	initial binning	σ_{100}	optimized binning	σ_{op}
S0		3.72	[0, 400, 590, 1000]	2.82
S1		1.74	[0, 590, 1000]	1.18
M0		3.76	[0, 410, 590, 1000]	2.72
M1		3.70	[0, 410, 590, 1000]	2.85
M7	[0, 10, ..., 990, 1000]	3.41	[0, 410, 590, 1000]	2.56
T0		4.05	[0, 590, 1000]	2.80
T1		4.06	[0, 590, 1000]	2.86
T2		3.14	[0, 410, 590, 1000]	2.50

Table 5.3: Development of bin edges and EFT significance for all operators of m_{ll} .

Table 5.4 depicts the significance of the EFT signal after the bin optimization for S0_8. An overview for all operators can be found in section 9. As expected the merging process led to

¹This is especially important for the statistics framework, which will be used to create the maximum likelihood fits. The SM events decrease for higher energies yet the fit break down for low statistics. So one has to make sure that the histograms provide a minimum number of background events in all bins.



(a) Starting point of the bin optimization.

(b) Binning after the bin optimization.

Figure 5.2: Demonstration of bin optimization algorithm for $S0_8$ and m_{ll} .

a loss of significance for all operators. The variable m_{o1} allows the highest EFT significance for most of the operators. Followed by m_T and m_{ll} these variables always result in higher significance's than R_{tp} , $\cos(\Delta\Phi_{leps})$, $\Delta\Phi_{jets}$. This confirms the study in [14], where it was found that the last two variables do not sufficiently discriminate the EFT events against the background. Therefore they will be excluded from further analysis. Since the significance for R_{tp} is also lower, it is also excluded.

	m_{o1}	m_T	m_{ll}	R_{tp}	$\cos(\Delta\Phi_{leps})$	$\Delta\Phi_{jets}$
σ_{op}	3.06	2.97	2.50	1.77	1.24	0.6

Table 5.4: optimized significance's for $S0_8$ and all variables.

In favour of simplicity, a general binning for each of the remaining variables is then chosen. As seen in Table 5.3 most of the operators already have bin edges at 0,410, 590 and 1000 TeV. For the operators which lack the bin edge at 410 TeV after the bin optimization, this additional edge is added in by hand. At this stage, each histogram contains 3 identical bins, which results in a relatively rough depiction of the kinematic distributions (see Figure 5.2b). To restore some of the physical shape of the distribution, the first bin is divided into several smaller bins. This can be done without much of a significance loss, since the EFT contributions increase for higher energies, and therefore most of the significance already comes from the last bin. Since the number of SM-predictions is high in this region, this can also be done without violating the minimal events condition. Figure 9.8 displays the final binning in case of $S0_8$ but apart from the EFT contributions the figure looks the same for all operators.

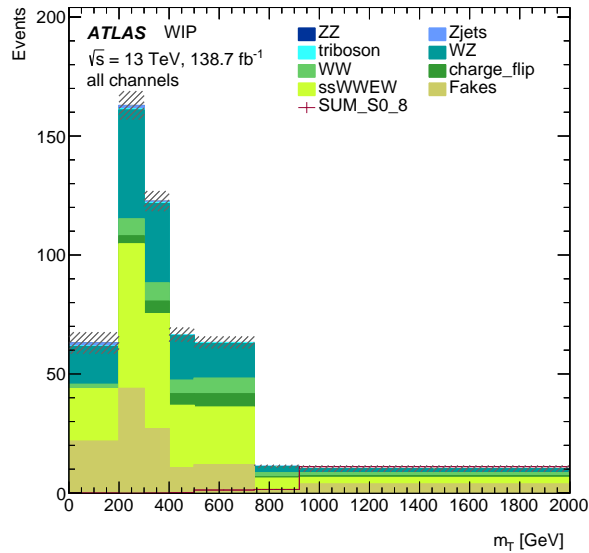
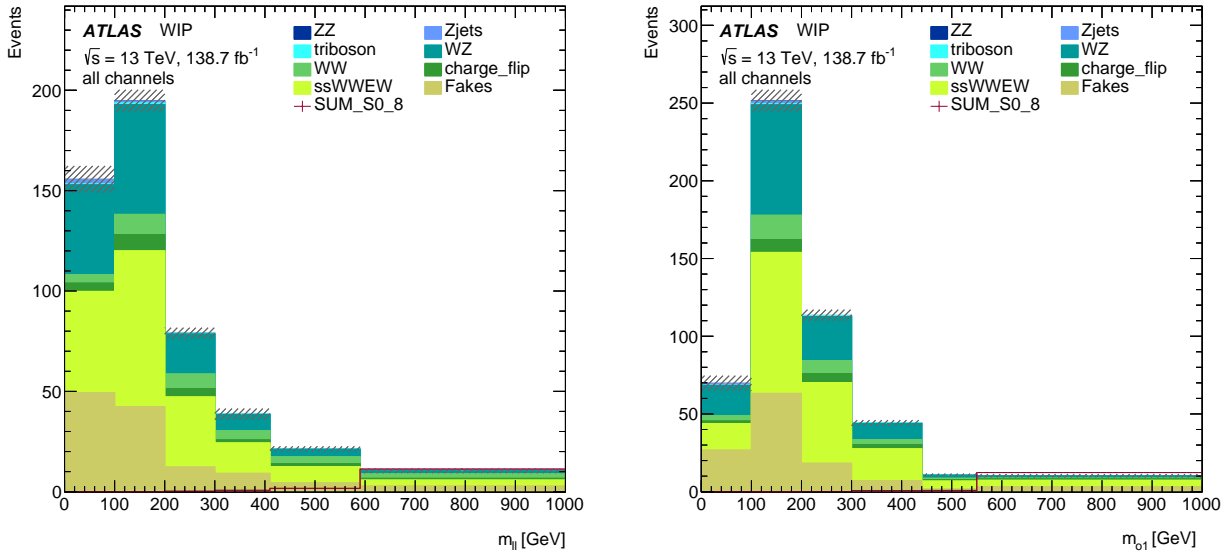


Figure 5.3: Final binning for the three remaining variables and S0_8.

	final binning
m_{ll}	[0, 100, 200, 300, 410, 590, 1000]
m_{o1}	[0, 100, 200, 300, 440, 550, 1000]
m_T	[0, 200, 300, 400, 500, 740, 920, 2000]

Table 5.5: Final binning for all operators.

6 Statistical Limits

After obtaining the bin optimization for the most sensitive variables, the goal is to receive the one σ and two σ limits for the Wilson coefficients. The limits are extracted using the EFTfun framework [19], which will perform Maximum Likelihood fits. Both section 6.1 and section 6.2 focuss on justifying the choices, which are made during the analysis. As data the so called 'asimov' dataset is used. In this set, all observed quantities are set equal to their expected values and the uncertainty is chosen according to poisson statistic. In a sense, it can be seen as the single most representative data set for SM predictions. The probability density function results from the Effective Lagrangian. Ideally, one would be able to vary all operators of a given subset at the same time. But for the currently available statistics, this aim is more than ambiguous. Instead, the focus is set on determining the limits for each operator individually. This is achieved by setting all non-corresponding coefficients to zero.

6.1 Statistical limits for the Different Variables

In a first step the limits are extracted for each of the remaining variables.

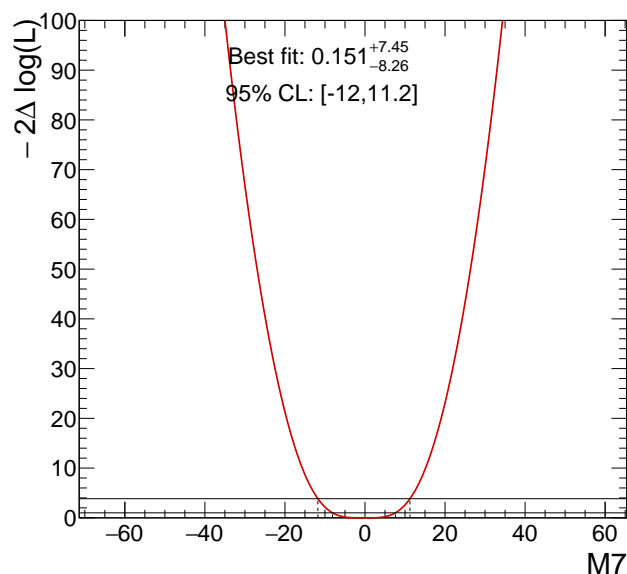


Figure 6.1: Logarithmic Maximum Likelihood Function for $M7$ and m_{ll} . The straight and dashed lines resemble the 1 and 2 σ limits.

Once performed, the program returns the logarithmic Maximum Likelihood Function for each operator, variable and clipping value. An exemplary depiction is shown in Figure 6.1. All fits have parabolic shape with a minimum close to zero. This is expected since we fit the Wilson coefficients to asimov data. The slope, however, varies from function to function resulting in different limits for each of the Maximum Likelihood fits. An overview of the 2σ limits is presented in Table 6.1. The three variables show very similar limits. No major variations are reported.

	m_{o1}		m_{ll}		m_T	
M0	-4.96	4.93	-5.08	5.02	-4.90	4.84
M1	-7.1	7.74	-7.69	8.21	-7.29	7.72
M7	-11.17	10.53	-11.77	11.24	-11.18	10.72
S1	-24.86	25.64	-25.52	26.25	-25.87	26.4
S0	-6.07	6.31	-6.37	6.59	-6.43	6.6
T0	-0.46	0.49	-0.47	0.5	-0.45	0.48
T1	-0.2	0.24	-0.22	0.24	-0.21	0.24
T2	-0.62	0.81	-0.71	0.89	-0.64	0.81

Table 6.1: $\pm 2\sigma$ limits for each operator and variables

6.2 Statistical Limits for Different Binnings

There have been previous efforts by the ATLAS group to extract the limits using the same EFTfun framework [20]. Their note is more broadly based as it includes both the limits for $W^\pm W^\pm jj$ and $W^\pm Zjj$ channel. Additionally, they extract the limits for a combination of the two, taking into account the correlations between the two channels. Systematic and statistical uncertainties are included, while this study only considers statistical uncertainties. The study builds on the partial 36fb^{-1} data from RUN 2, where here the full 139fb^{-1} RUN 2 is implemented. Their research only uses the variable m_{ll} focussing on the lower end of the energy spectrum:

previous binning [20, 80, 130, 170, 220, 320, 500]

The last bin is also an overflow bin. In comparison, the binning in this study goes up to 1 TeV:

binning in my thesis [0,100,200,300,410,590,1000]

	$\pm 2\sigma_{previous}$		$\pm 2\sigma_{thesis}$	
M0	-7.01	6.86	-5.08	5.02
M1	-10.12	10.87	-7.69	8.21
M7	-15.93	15.04	-11.77	11.24
S1	-33.94	35.29	-25.52	26.25
S0	-8.45	8.86	-6.37	6.59
T0	-0.65	0.70	-0.47	0.5
T1	-0.29	0.34	-0.22	0.24
T2	-0.90	1.15	-0.71	0.89

Table 6.2: Comparison between the binning used in [20] and in this thesis.

To check whether this energy expansion improves the limit measurements, one needs to remove all differing factors between the two studies. In the end, this means extracting the limits for the two different binning for the full RUN 2 datasets used previously in this thesis. Table 6.2 summarizes the results of the limit extraction. A decrease in the 2σ limits is observed.

6.3 Clipping Scan

As mentioned in section 3.4 EFT are not UV-complete. This can again be compared with the Taylor expansion analogy in Figure 3.2. An expansion is only able to accurately describe the function $f(x)$ within a specific range. Above that range, the deviations become undeniable. In the case of EFT operators, it is demanded that the ssWW sub-process cross section does not exceed the total proton-proton cross section. If this criteria is not satisfied by the EFT, it won't predict physical processes with great accuracy. As a consequence, it is necessary to define a certain cut-off E_{cut} value after which the EFT predictions are set to zero while still keeping SM events, since these are already part of a consistent theory. This technique will be referred to as clipping and it's recommended by the anomalous gauge coupling taskforce [21] for the unitarisation of the BSM effects.

The objective in this part is to vary the cut-off scale and observe its effects on the statistical limits. This procedure is called clipping scan and it is performed by adding cuts into the cut flow of the CAF. The selection criteria will be performed on the truth level variable $m_{ll\nu\nu}^{truth}$, so before any detector simulations have taken place. It is identical to the invariant mass of the WW bosons m_{WW} and therefore mimics the center-of-mass energy of the scattering process. The clipping will be performed at 1, 1.5, 2 and 5 TeV. Additionally, the limits are also extracted for no cut off. This will be referred to as a clipping value of ∞ . Table 6.3 presents an overview of the amount of events, broken down to the specific operators. A cut at 5 TeV does not impact the number of events as drastically as the lower energy cuts. This shows,

$E_{cut}[TeV]$	S0_8	S1_20	M0_6	M1_10	M7_13	T0_0p6	T1_0p3	T2_1	ssWW EW
∞	13.644	5.126	14.100	14.494	13.829	12.120	12.234	12.379	189.20
5	13.411	5.029	13.689	13.937	13.409	11.208	10.918	10.860	189.20
2	4.892	1.706	5.667	3.921	5.376	2.685	0.984	-0.146	189.10
1.5	2.115	0.646	3.713	1.796	3.404	1.526	0.275	-0.749	188.62
1	0.334	-0.008	2.370	0.740	1.965	1.120	0.468	-0.097	184.82

Table 6.3: Amount of events broken down to the specific operators at given cut-off energy E_{cut} . To see how the ssWW electroweak predictions compare, the amount of SM events below a certain energy threshold are presented as well, even though those will not be cut off.

that most of the EFT events lie in between 1 and 5 TeV, which justifies the chosen clipping range. The negative entries can be explained as followed: The events are calculated from the sum of the interference and quadratic term of each operator. The interference term alone can lead to negative contributions, while the quadratic is always positive. For higher energies, the quadratic term is expected to be dominant [14]. Thus, a cut on higher energies affects the quadratic events more, resulting in a negative sum. At energies above 1.5 TeV the expected SM events are already expected to be below one.

CAF then allows access to all histograms at different cut-flow levels, which are then transferred into the EFT fitting tool. These results are then compared to the unitarity bounds which were introduced earlier in section 3.5. Since the limits are derived for each operator individually, they are compared with the theory line for only one operator (see Table 3.2). The interest lies in the intersection between the unitarity bounds and the 2σ limits. If the unitary bounds are inside the 2σ environment, the operator violates unitarity for the considered energy. If it falls outside these limits, it does not. Since the upper and lower limits are not identical, the minimum intersection value is chosen. This can be seen in Figure 6.2 for M7 and m_U and in section 9 for the rest of the operator-variable combinations.

Apart from S1, each of the operators show a range of validity between 1 and 2.5 TeV. A summary of all minimum intersection points can be seen in Table 6.4. For S1, no intersection

	maximum validity [TeV]		
	m_U	m_{o1}	m_T
S0	1.60	1.65	1.59
S1	-	-	-
M0	1.26	1.29	1.30
M1	1.69	1.75	1.75
M7	1.86	1.92	1.91
T0	1.55	1.60	1.55
T1	2.35	2.38	2.39
T2	1.78	1.84	1.86

Table 6.4: Validity in regards to unitarity for all operators and variables.

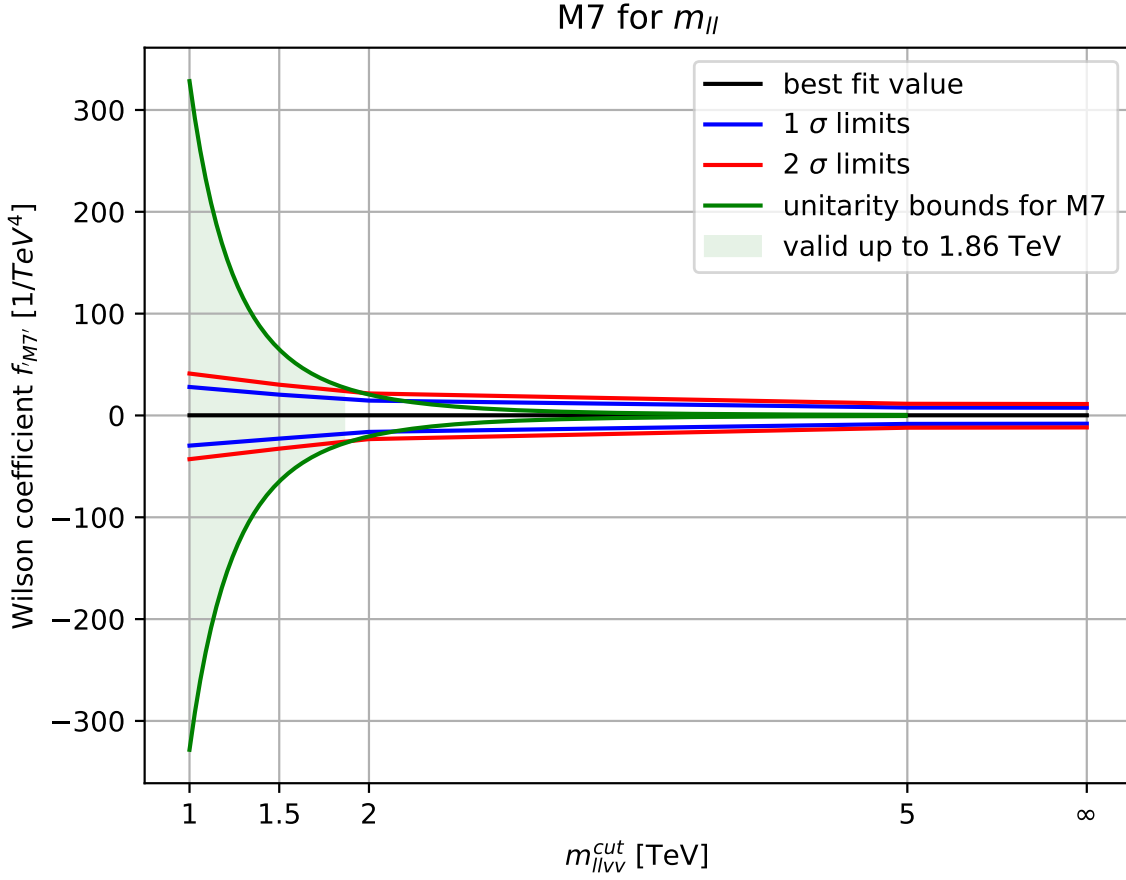


Figure 6.2: Comparison between the results from the maximum likelihood fit (black, blue and red line) and the theory unitarity bounds (green line) for M7. The light green area marks the region of validity. The last entry at ∞ represents the limits for no performed clipping.

could be determined, since the theory bounds fall in between the 2σ limits for all clipping values. This was somewhat expected since S1 showed by far the smallest signal significance of all operators in section 5.2. This shows, that the sensitivity of the analysis of S1 is still quite poor. The three remaining variables m_{II} , m_{o1} and m_T performed equally. Apart from small variations, none of the examined variables show significantly higher validity ranges than the other.

7 Summary and Outlook

This thesis focussed on providing a validity range for 8 different EFT operators. These operators are of special interest since they affect the $ssWW$ scattering amplitude. Before obtaining the limits, the histograms needed to be adjusted to suit the analysis framework. This includes determining variables which are sensitive to the individual operators. The variables m_{ll} , m_{o1} and m_T have proven to be almost equally sensitive to the individual operators. R_{tp} , $\Delta\phi_{jets}$ and $\cos(\Delta\Phi_{leps})$ on the other hand did not show the required significance and were therefore excluded from further analysis. Following a bin optimization algorithm, an optimal binning for each of these variables was introduced. In a next step, the one and two σ limits for different clipping values were calculated. Comparing these results with the theoretical unitarity bounds led to identifying a specific maximum center-of-mass energy where these operators do not violate unitarity. The results are summarized in Table 6.4. S1 is the only operator which couldn't provide a range of validity. It also showed the least signal significance during the bin optimization.

However, the results in this thesis can only be seen as temporarily, but its outcome motivates subsequent research. After determining a range of validity for the EFT operators, the next goal is to set the limits for the Wilson coefficient for a clipping value inside the unitarity bounds. The optimal clipping value should be discussed inside the $W^\pm W^\pm \rightarrow W^\pm W^\pm$ research community. There are two main points in this discussion. Firstly, a reasonable candidate for E_{cut} would be the intersection point for each operator, but this would lead to a different clipping values for each of the operators. Secondly, the clipping value E_{cut} should be in a range, where the expected SM predictions are close to zero (see Table 6.3). Extracting the limits for the final clipping value also includes to reevaluate the optimal binning. In this study, the optimization was accomplished without any cut-off of EFT events. The same binning was used for all the clipping values. Since the harshest criteria in the bin optimization algorithm is the number of SM backgrounds events, the binning is not expected to differ much. Afterwards, the limits for this binning can be calculated. Further, this study only included statistical uncertainties. In a next step, one should include systematic uncertainties into the limit measurement. This will most likely increase the one and two σ limits. It would be interesting to see whether the limits still show an intersection point with the unitarity bounds. These results would provide a more complete picture on the calculated limits.

Erklärung

Hiermit erkläre ich, dass ich diese Arbeit im Rahmen der Betreuung am Institut für Kern- und Teilchenphysik ohne unzulässige Hilfe Dritter verfasst und alle Quellen als solche gekennzeichnet habe.

Pia Marie Müller
Dresden, März 2022

Acknowledgements

At first, I'd like to thank Frank Siegert for offering me the possibility to work in the field of particle physics. The three months I spend in this working group were enjoyable, despite the unfortunate conditions. The weekly coffee chats offered with all the group members provided a nice change to the everyday corona live and made me feel welcomed in the working group. Another big thank you goes to Joany Manjarres Ramos, who accompanied this work thematically and therefore introduced me into the world of modern particle physics. Last but not least, a special thanks to Max Stange, who always had an open ear for my questions and sometimes spent hours trying to fix errors together with me.

8 Bibliography

- [1] Lyndon R Evans and Philip Bryant. “LHC Machine”. In: *JINST* 3 (2008). This report is an abridged version of the LHC Design Report (CERN-2004-003), S08001. 164 p. DOI: 10.1088/1748-0221/3/08/S08001. URL: <https://cds.cern.ch/record/1129806>.
- [2] The ATLAS Collaboration, G Aad, E Abat, et al. “The ATLAS Experiment at the CERN Large Hadron Collider”. In: *Journal of Instrumentation* 3.08 (Aug. 2008), S08003–S08003. DOI: 10.1088/1748-0221/3/08/s08003. URL: <https://doi.org/10.1088/1748-0221/3/08/s08003>.
- [3] Joao Pequeno. “Computer generated image of the whole ATLAS detector”. Mar. 2008. URL: <https://cds.cern.ch/record/1095924>.
- [4] Manjarres, Joany and Stange, Max and Herrmann, Tim. *Little introduction to Vector Boson Scattering and New physics searches with Effective Field Theory*. Mar. 25, 2021.
- [5] Raquel Gomez-Ambrosio. “Studies of Gauge Couplings at LHC: the Effective Field Theory Approach”. PhD thesis. Oct. 2017. DOI: 10.13140/RG.2.2.23472.87049.
- [6] Céline Degrande, Nicolas Greiner, Wolfgang Kilian, et al. “Effective field theory: A modern approach to anomalous couplings”. In: *Annals of Physics* 335 (Aug. 2013), pp. 21–32. DOI: 10.1016/j.aop.2013.04.016. URL: <https://doi.org/10.1016%2Fj.aop.2013.04.016>.
- [7] Carsten Bittrich. “Evidence for Scattering of Electroweak Gauge Bosons in the $W^\pm Z$ Channel with the ATLAS Detector at the Large Hadron Collider”. Presented 14 Jul 2020. PhD thesis. 2020. URL: <https://cds.cern.ch/record/2719126>.
- [8] Carsten Bittrich, William Kennedy Di Clemente, Emily Marie Duffield, et al. *Support note for measurement of electroweak $W^\pm W^\pm jj$ production at $\sqrt{s} = 13$ TeV*. Tech. rep. Geneva: CERN, Mar. 2018. URL: <https://cds.cern.ch/record/2309552>.
- [9] O. J. P. Éboli, M. C. Gonzalez-Garcia, and J. K. Mizukoshi. “ $pp \rightarrow jje^\pm \mu^\pm$ and $jje^\pm \mu^\mp$ at $\mathcal{O}(\alpha_{em}^4)$ and $\mathcal{O}(\alpha_{em}^4 \alpha_s^2)$ for the Study of the Quartic Electroweak Gauge Boson Vertex at LHC”. In: *Physical Review D* 74.7 (Oct. 2006). ISSN: 1550-2368. DOI: 10.1103/PhysRevD.74.073005. URL: <http://dx.doi.org/10.1103/PhysRevD.74.073005>.

-
- [10] Eduardo da Silva Almeida, O. J. P. Éboli, and M. C. Gonzalez–Garcia. “Unitarity constraints on anomalous quartic couplings”. In: *Physical Review D* 101.11 (June 2020). ISSN: 2470-0029. DOI: 10.1103/physrevd.101.113003. URL: <http://dx.doi.org/10.1103/PhysRevD.101.113003>.
- [11] Andy Buckley, Jonathan Butterworth, Stefan Gieseke, et al. “General-purpose event generators for LHC physics”. In: *Physics Reports* 504.5 (July 2011), pp. 145–233. ISSN: 0370-1573. DOI: 10.1016/j.physrep.2011.03.005. URL: <http://dx.doi.org/10.1016/j.physrep.2011.03.005>.
- [12] Martin Erdmann, Thomas Hebbeker, and Alexander Schmidt. *Statistische Methoden in der Experimentalphysik*. Pearson, 2019.
- [13] ATLAS Group. *Common Analysis Framework*. URL: <https://atlas-caf.web.cern.ch/>.
- [14] Jonas Wagner. “Auswirkungen von Dim-8 Operatoren auf die Streuung gleich-geladener W-Bosonen und Suche nach sensitiven Observablen für deren Interferenz mit dem Standardmodell”. Bachelor’s Thesis. June 2021.
- [15] A. J. Barr, T. J. Khoo, P. Konar, et al. “Guide to transverse projections and mass-constraining variables”. In: *Physical Review D* 84.9 (Nov. 2011). ISSN: 1550-2368. DOI: 10.1103/physrevd.84.095031. URL: <http://dx.doi.org/10.1103/PhysRevD.84.095031>.
- [16] Stefanie Todt. “Investigation of mass reconstruction techniques for resonances in the scattering of $W^\pm W^\pm \rightarrow W^\pm W^\pm$ at the LHC”. Presented 04 Jun 2015. PhD thesis. Jan. 2015. URL: <https://cds.cern.ch/record/2000966>.
- [17] ATLAS Collaboration. “Differential cross-section measurements for the electroweak production of dijets in association with a Z boson in proton–proton collisions at ATLAS”. In: *The European Physical Journal C* (Feb. 2021). URL: <https://atlas.web.cern.ch/Atlas/GROUPS/PHYSICS/PAPERS/STDM-2017-27/>.
- [18] Yongsheng Gao, Liang Lu, and Xinlei Wang. “Significance calculation and a new analysis method in searching for new physics at the LHC”. In: *The European Physical Journal C* 45.3 (Dec. 2005), pp. 659–667. ISSN: 1434-6052. DOI: 10.1140/epjc/s2005-02456-9. URL: <http://dx.doi.org/10.1140/epjc/s2005-02456-9>.
- [19] Hannes Mildner. *EFTfun Framework*. 2020. URL: <https://gitlab.cern.ch/eft-tools/eft-fun/-/tree/ssWW>.
- [20] Tim Herrmann, Erini Kasimi, Michael Kobel, et al. “Combined effective field theory interpretation of $W^\pm W^\pm jj$ and $W^\pm Z jj$ measurements using ATLAS 13 TeV data”. Feb. 2022.

-
- [21] Andrea Bocci, Lucia Di Ciaccio, Dimitrios Iliadis, et al. “Recommendations from the Anomalous Gauge Coupling Taskforce”. June 2017. URL: <https://cds.cern.ch/record/2261444/files/ATL-COM-PHYS-2017-433.pdf>.

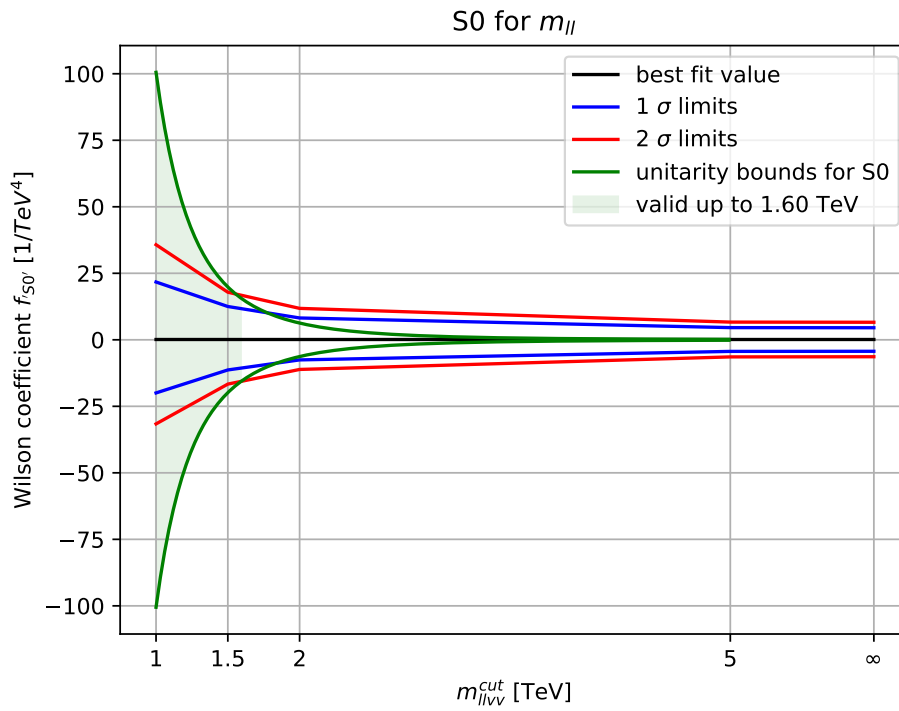
9 Appendix

Bin optimization significances

	m_{ll}	m_{o1}	R_{tp}	$\Delta\Phi_{jets}$	$\cos(\Delta\Phi_{leps})$	m_T
$S0$	2.82	3.09	2.67	0.64	1.26	2.76
$S1$	1.19	1.26	1.08	0.21	0.48	1.15
$M0$	2.72	2.86	2.13	0.65	1.16	2.85
$M1$	2.85	3.23	2.29	0.74	1.25	3.23
$M7$	2.56	2.90	2.14	0.70	1.09	2.73
$T0$	2.79	2.90	2.08	0.58	1.12	2.93
$T1$	2.86	3.11	2.29	0.59	1.21	3.03
$T2$	2.50	3.06	1.77	0.60	1.24	2.96

Table 9.1: Optimized significances for all operators and variables.

Comparison between unitarity bounds and limits from the maximum likelihood fits



(a) Clipping scan for m_{II} .

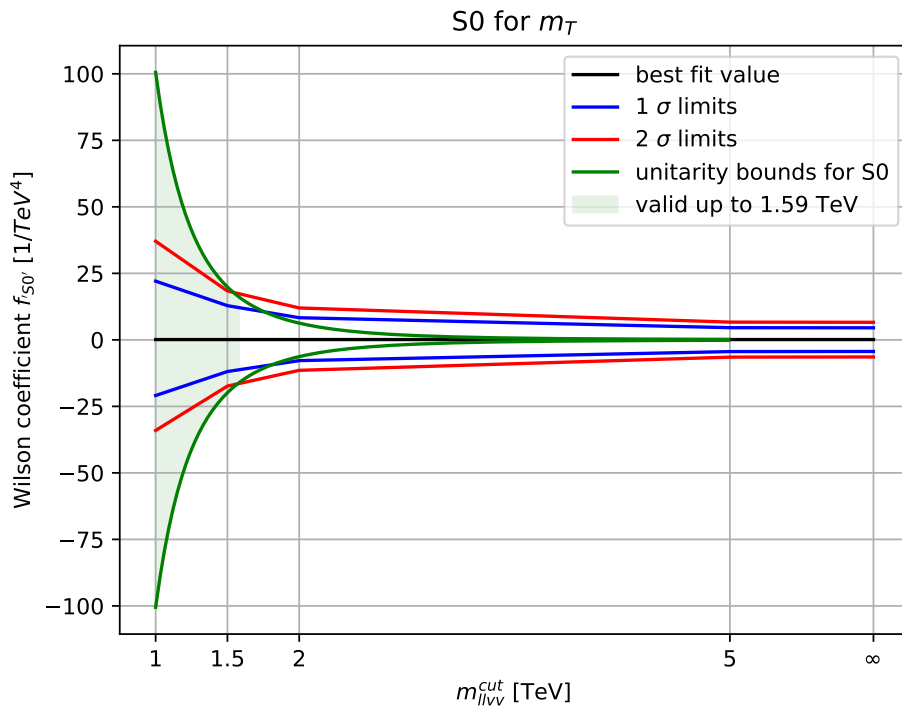
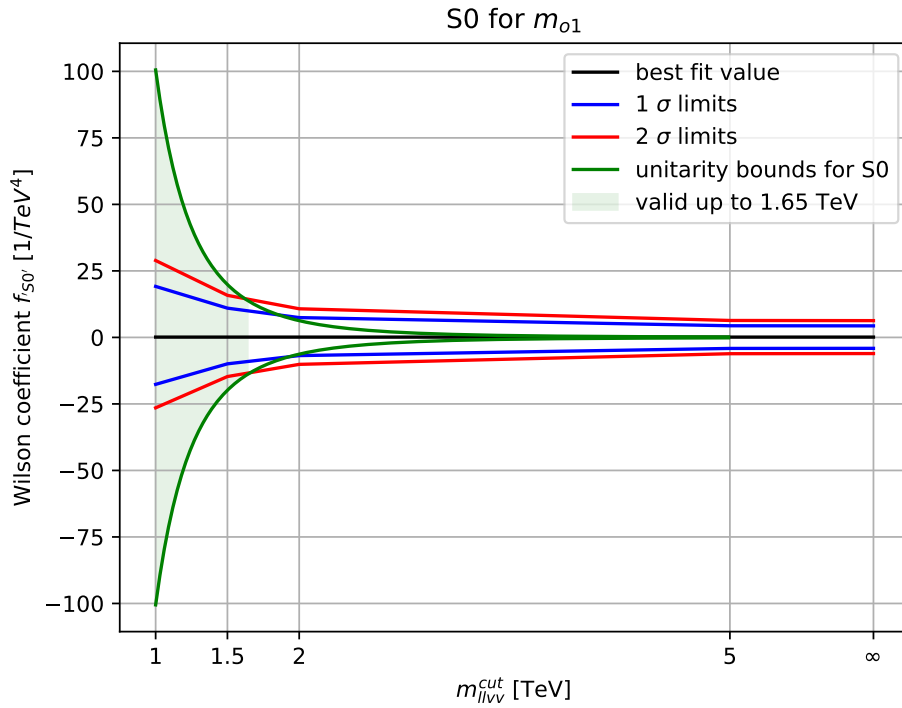
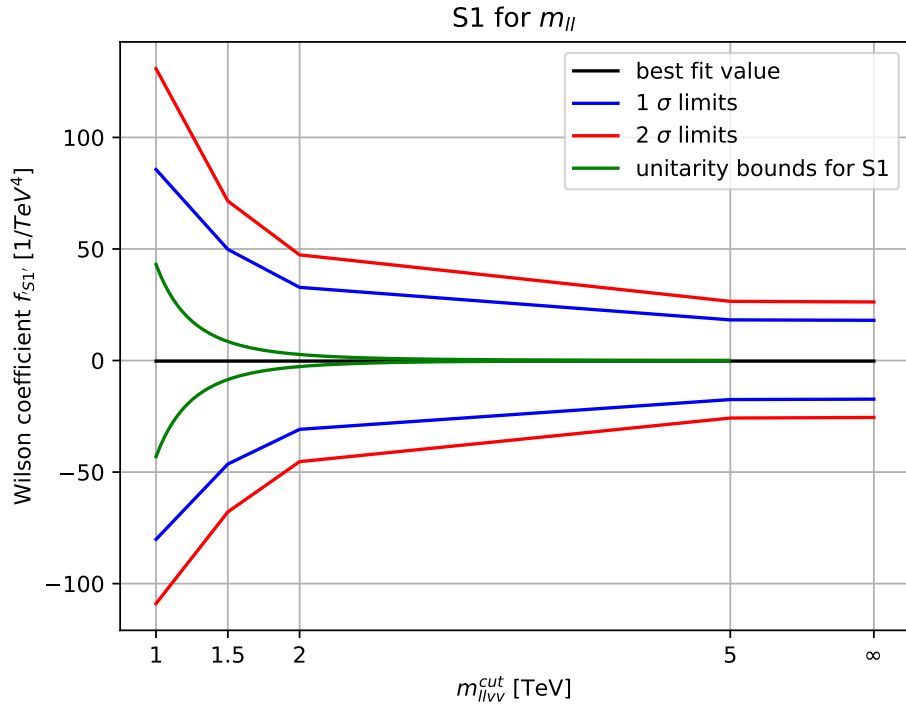
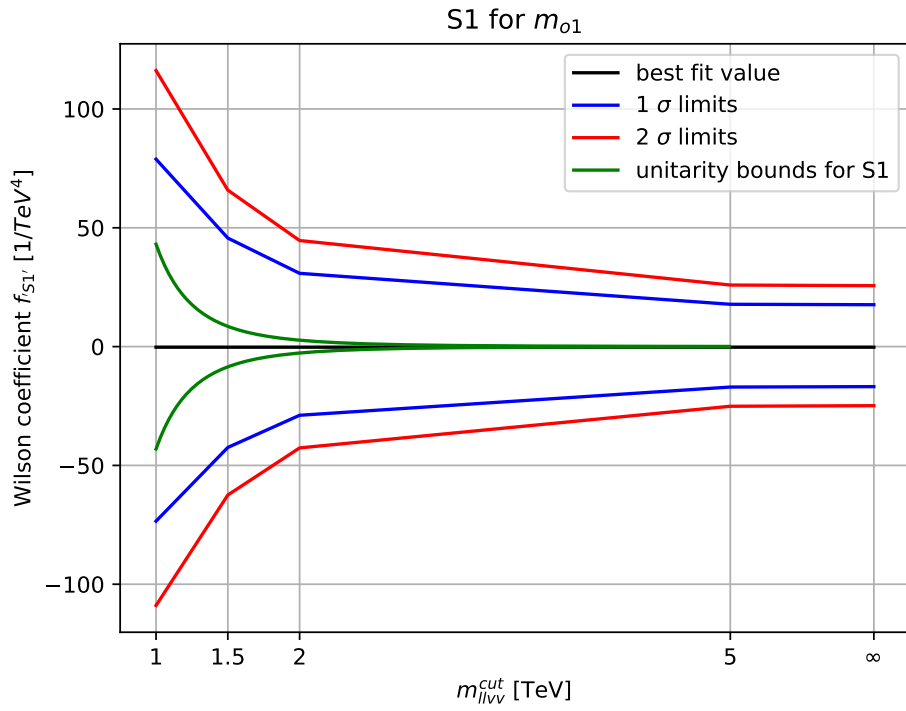


Figure 9.1: Limit depiction of Maximum Likelihood fits for S0 in comparison to unitarity bounds. The green area marks the validity range for this operator concerning unitarity.

(a) Clipping scan for m_{II} .(b) Clipping scan for m_{o1} .

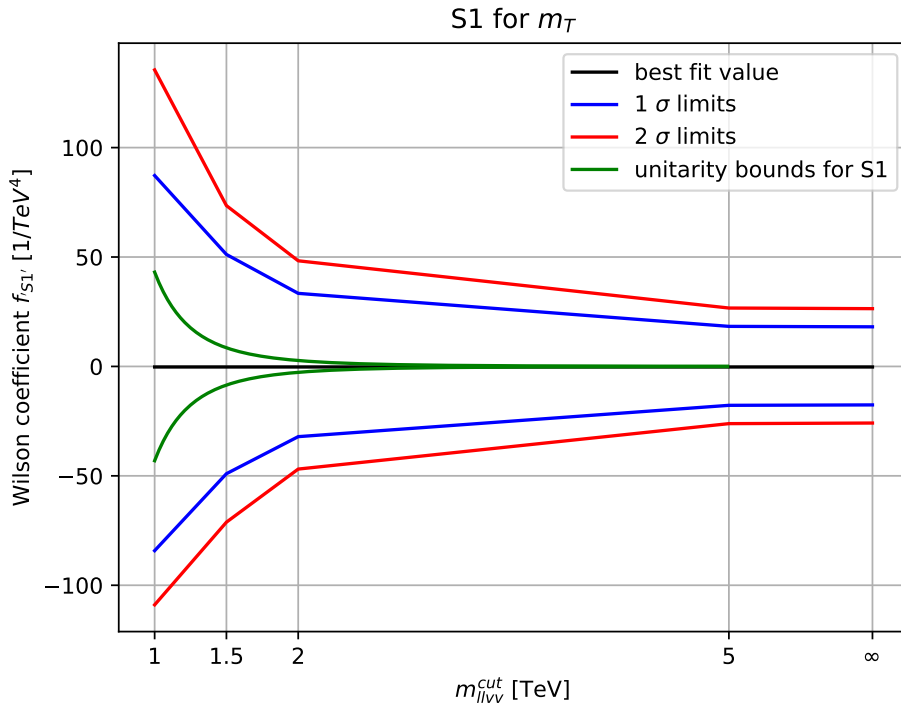
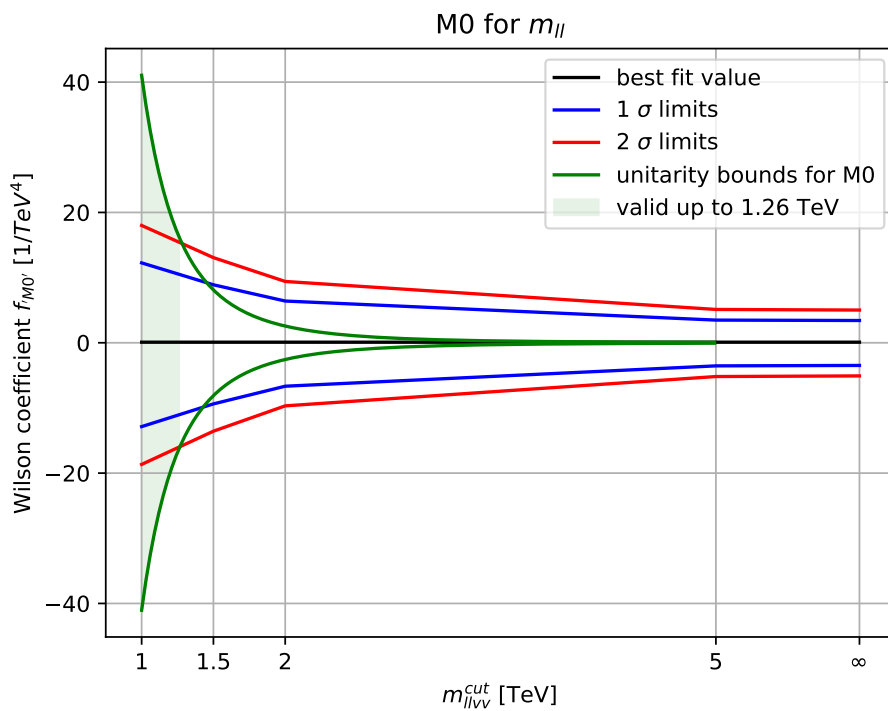
(c) Clipping scan for m_T .

Figure 9.2: Limit depiction of Maximum Likelihood fits for S1 in comparison to unitarity bounds. The unitarity bounds remain inside the statistical limits for all clipping values. No validity range could be detected.

(a) Clipping scan for m_{ll} .

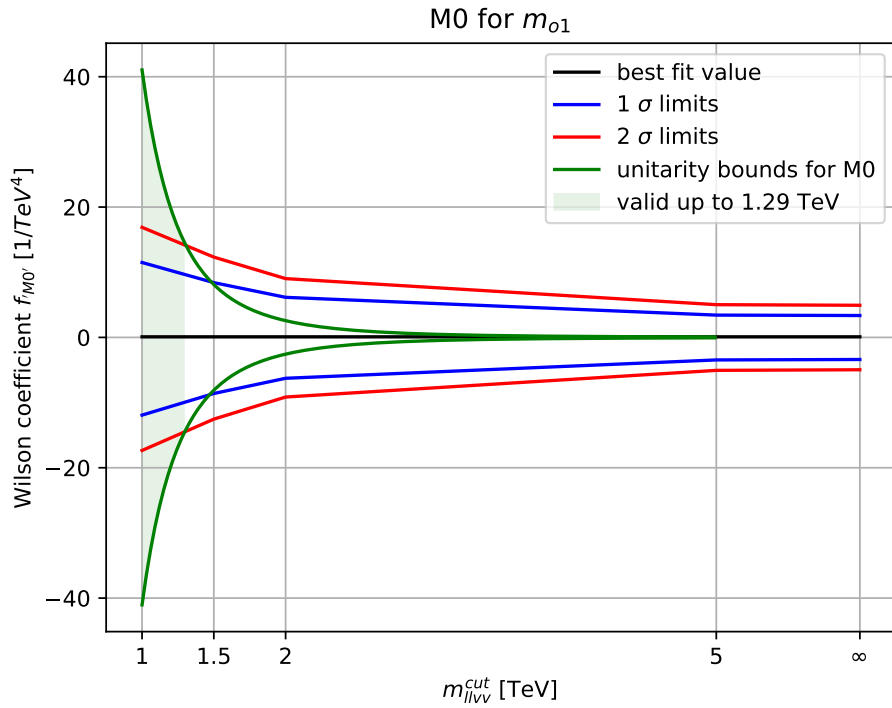
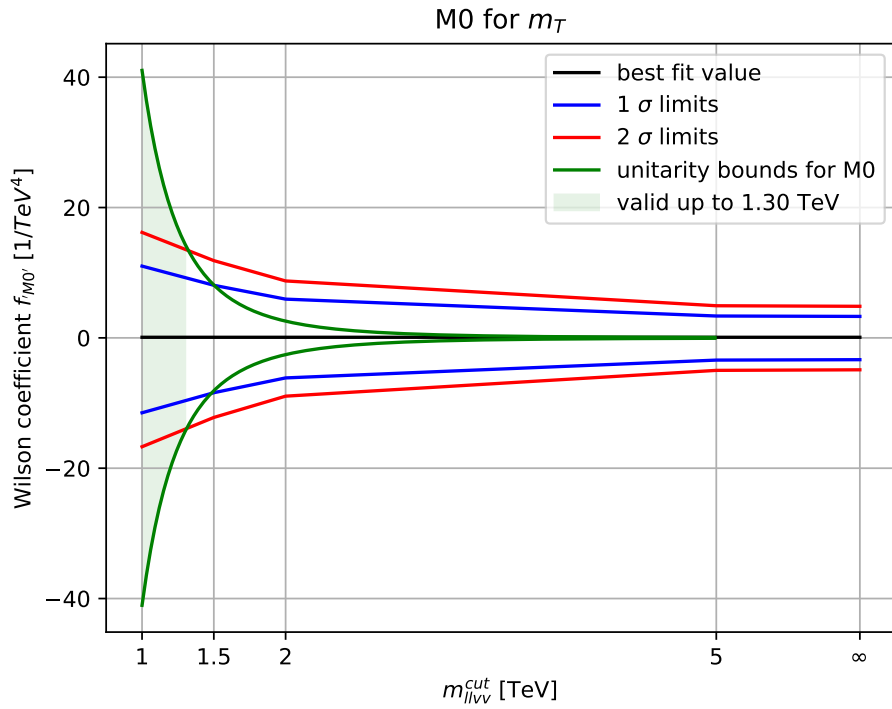
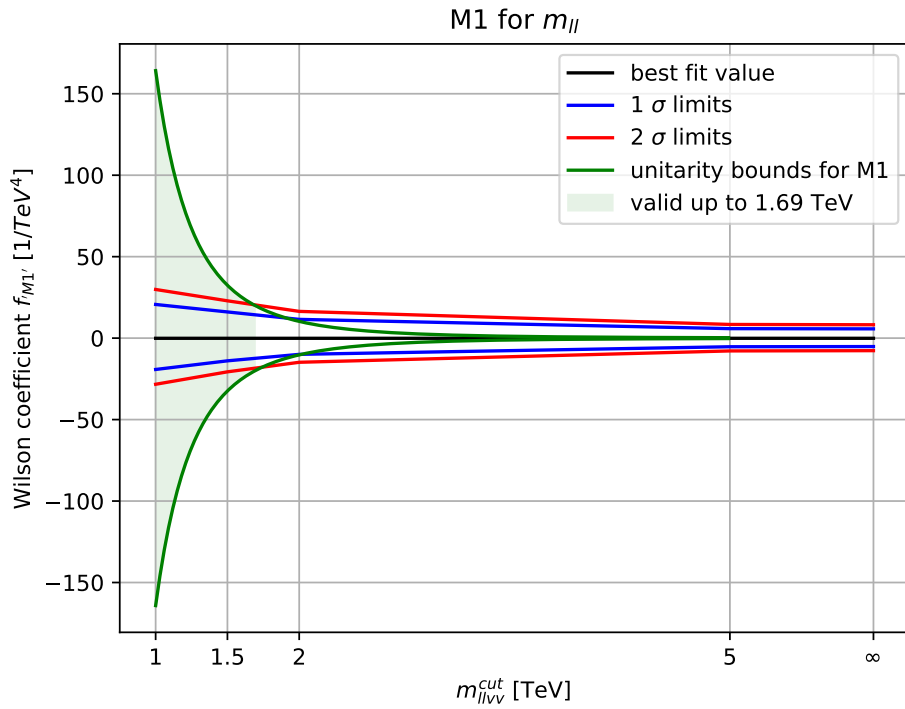
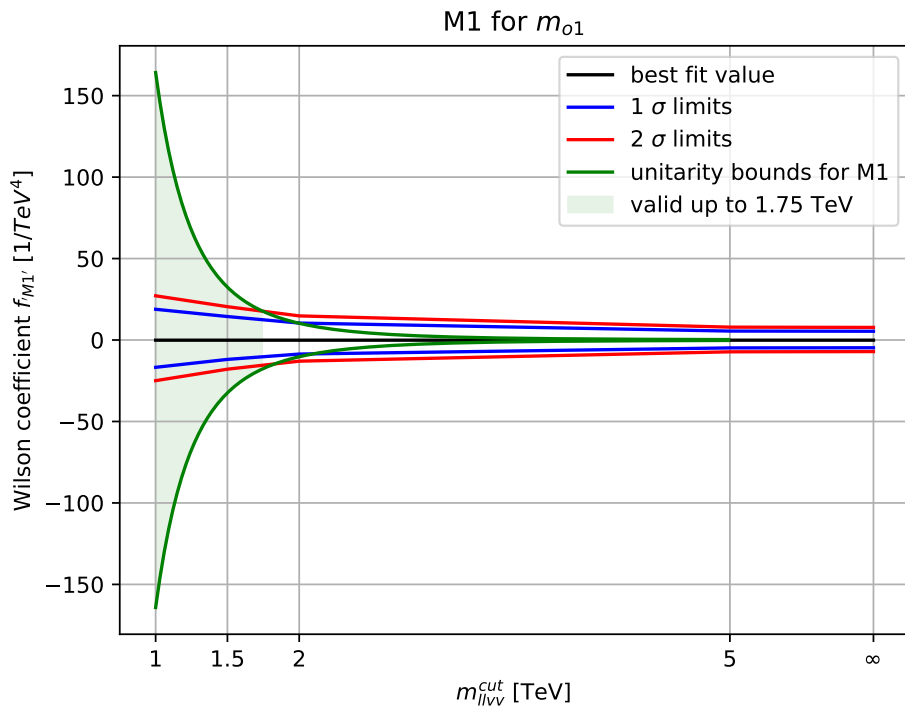
(b) Clipping scan for m_{o1} .(c) Clipping scan for m_{τ} .

Figure 9.3: Limit depiction of Maximum Likelihood fits for M0 in comparison to unitarity bounds. The green area marks the validity range for this operator concerning unitarity.

(a) Clipping scan for m_{II} .(b) Clipping scan for m_{o1} .

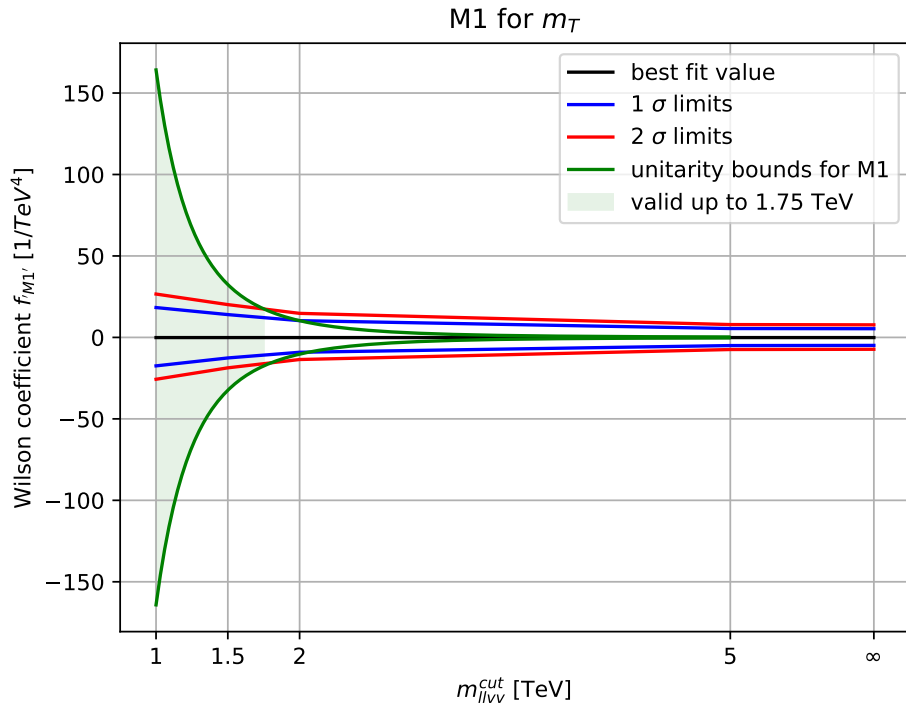
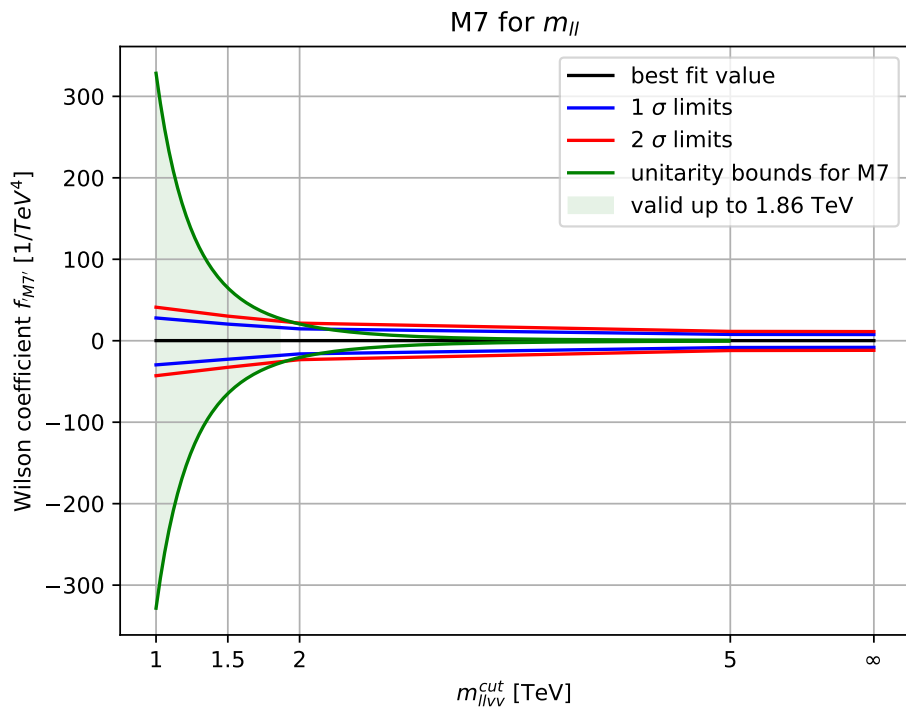


Figure 9.4: Limit depiction of Maximum Likelihood fits for M1 in comparison to unitarity bounds. The green area marks the validity range for this operator concerning unitarity.



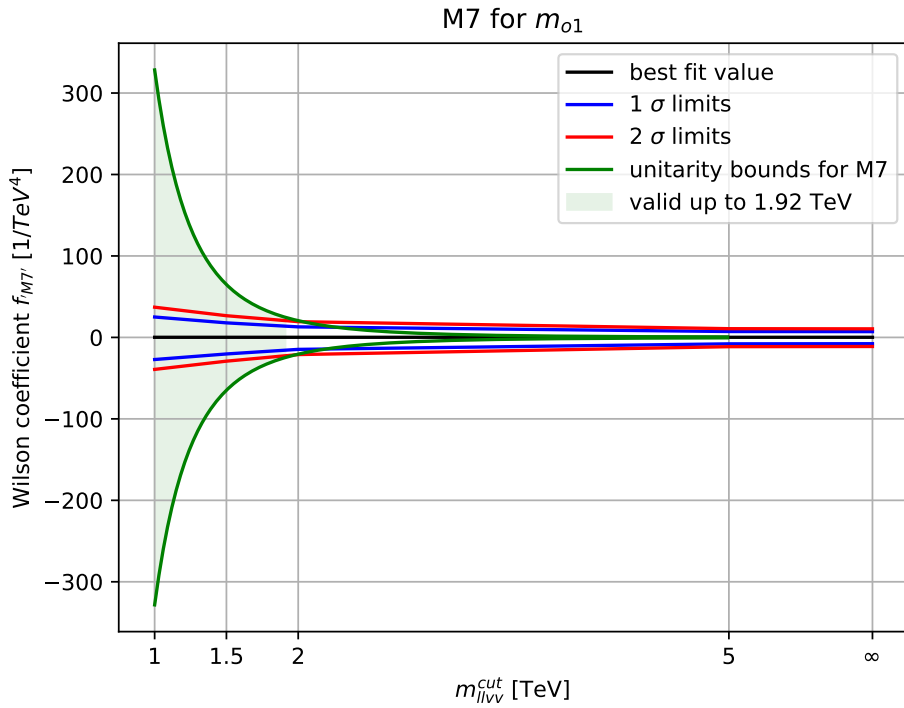
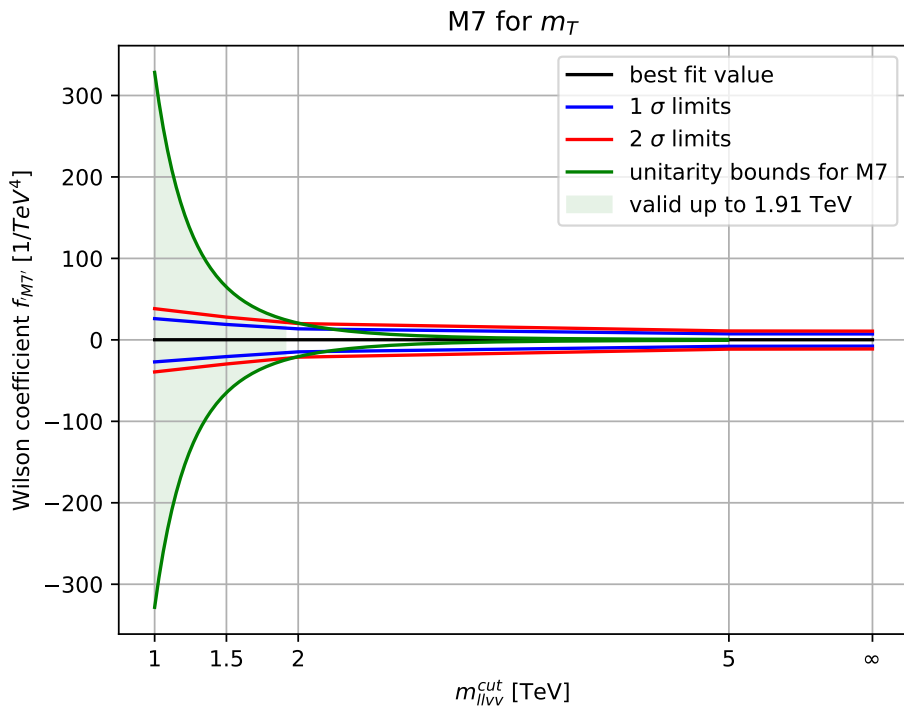
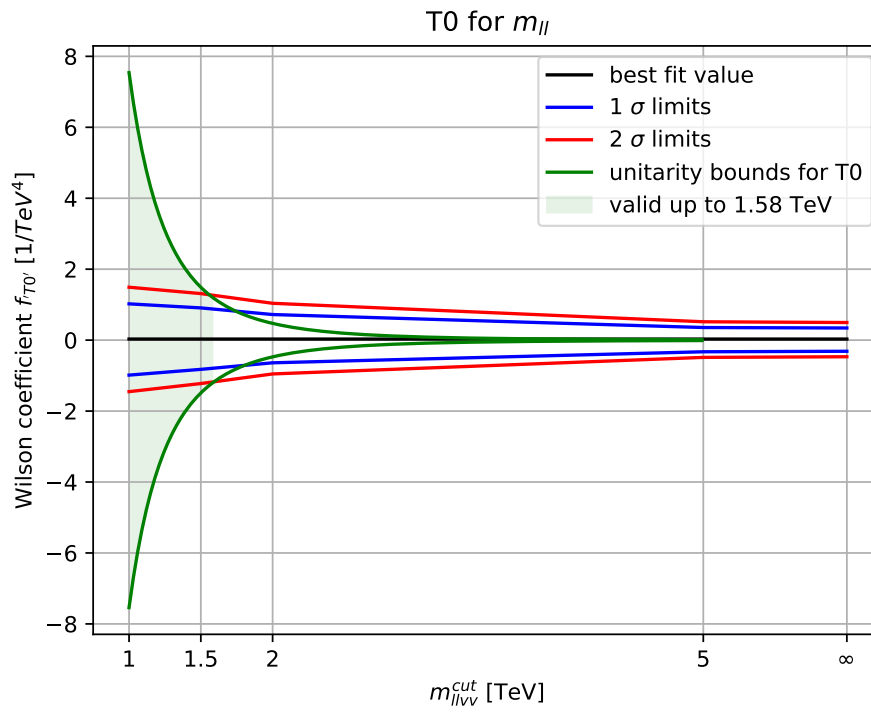
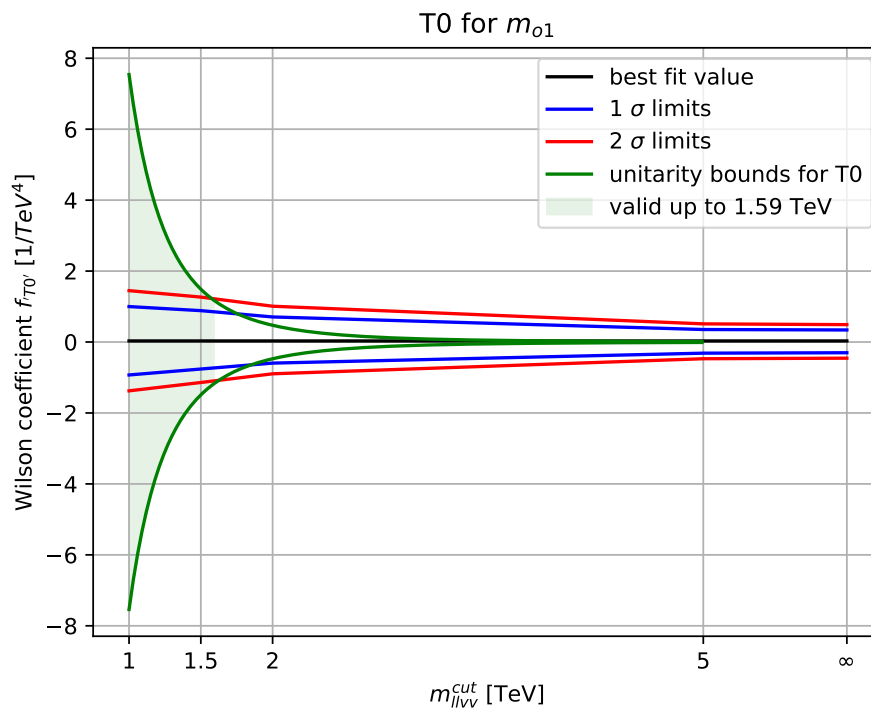
(b) Clipping scan for m_{o1} .(c) Clipping scan for m_T .

Figure 9.5: Limit depiction of Maximum Likelihood fits for M7 in comparison to unitarity bounds. The green area marks the validity range for this operator concerning unitarity..

(a) Clipping scan for m_{II} .(b) Clipping scan for m_{o1} .

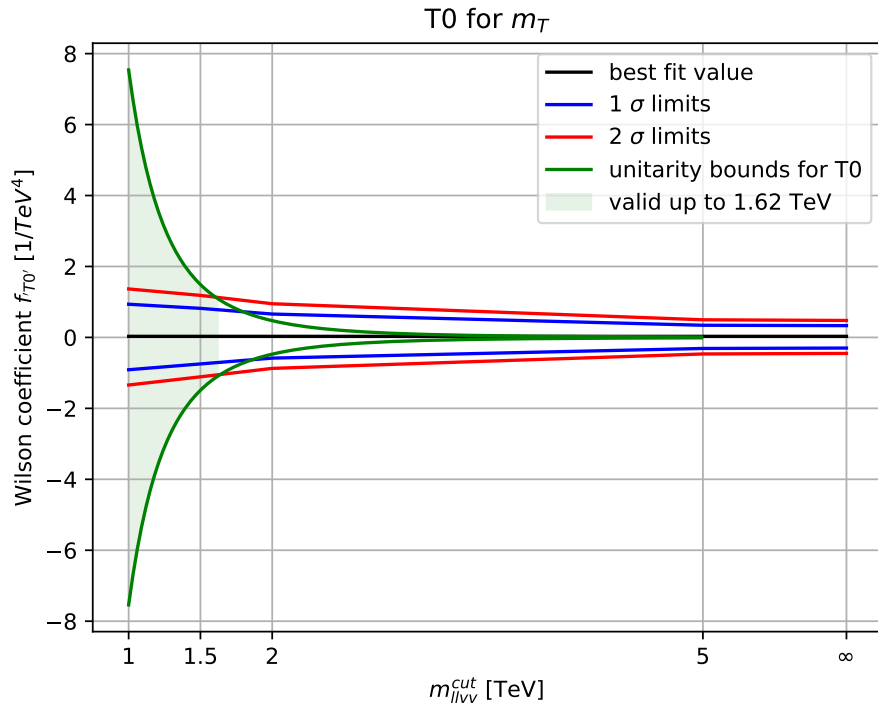
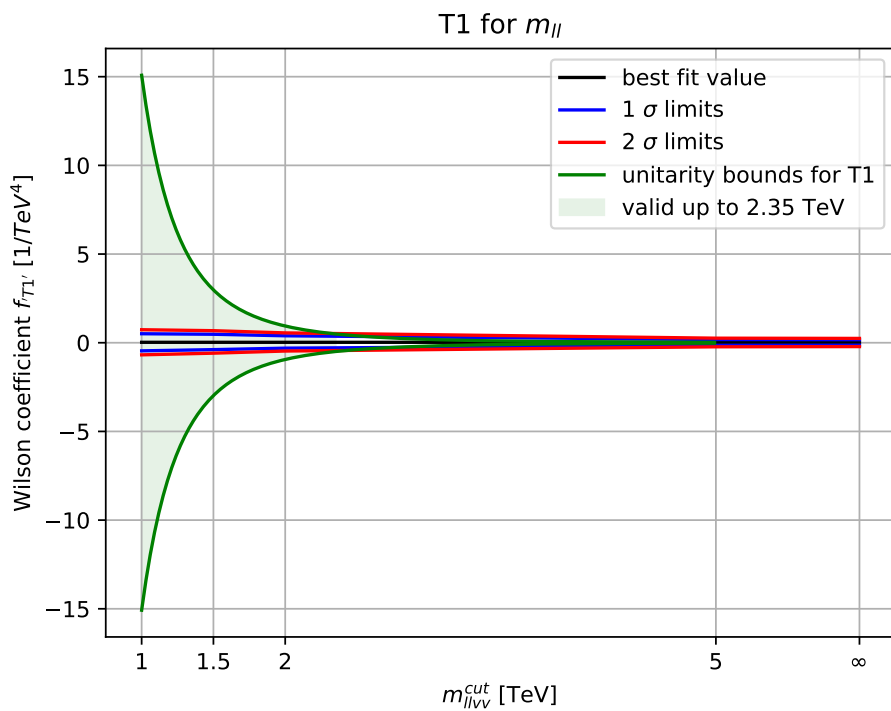
(c) Clipping scan for m_T .

Figure 9.6: Limit depiction of Maximum Likelihood fits for T0 in comparison to unitarity bounds. The green area marks the validity range for this operator concerning unitarity..

(a) Clipping scan for m_{II} .

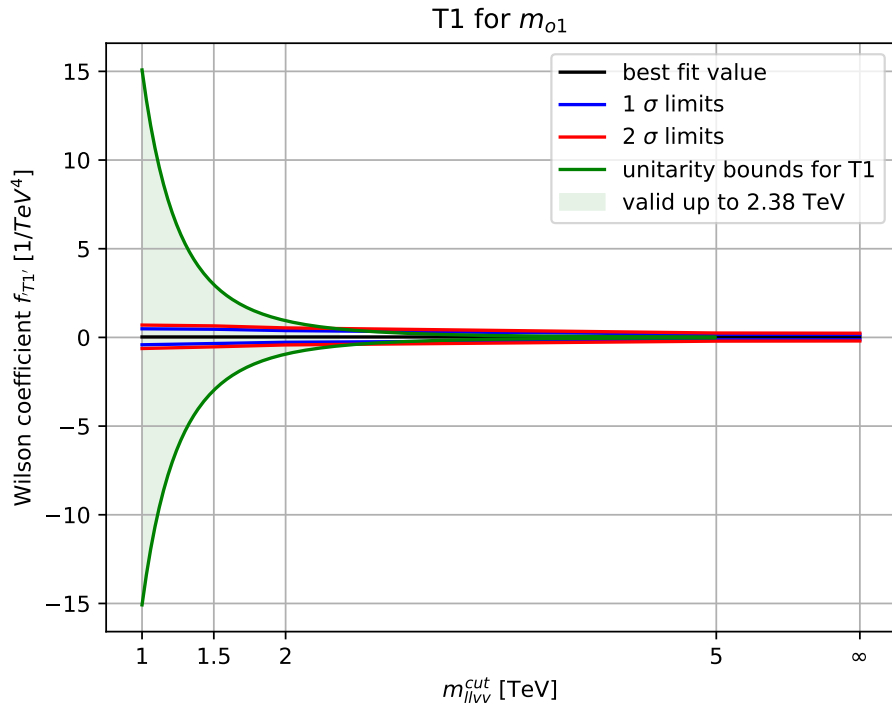
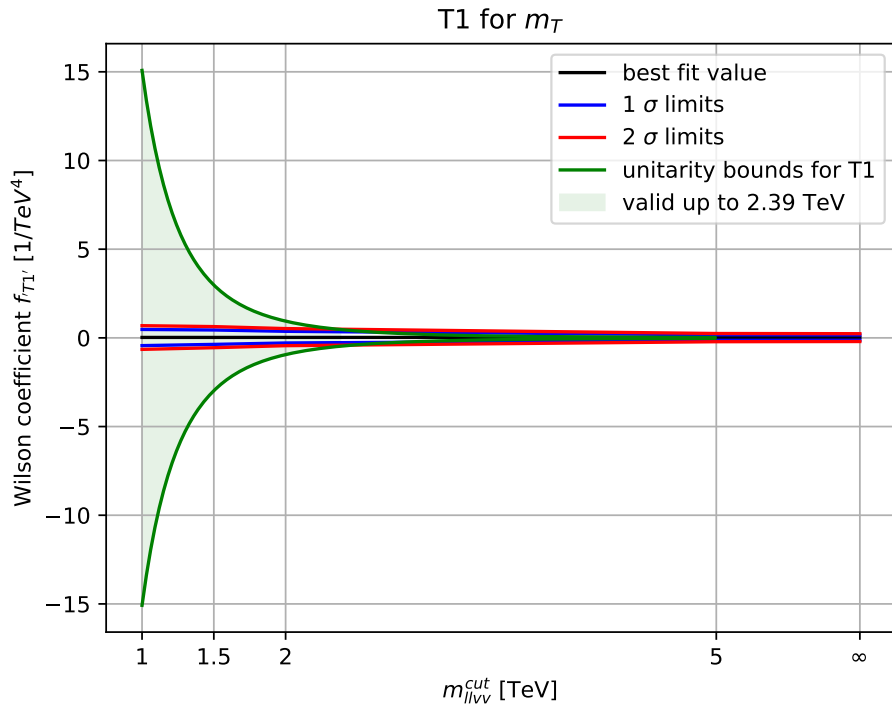
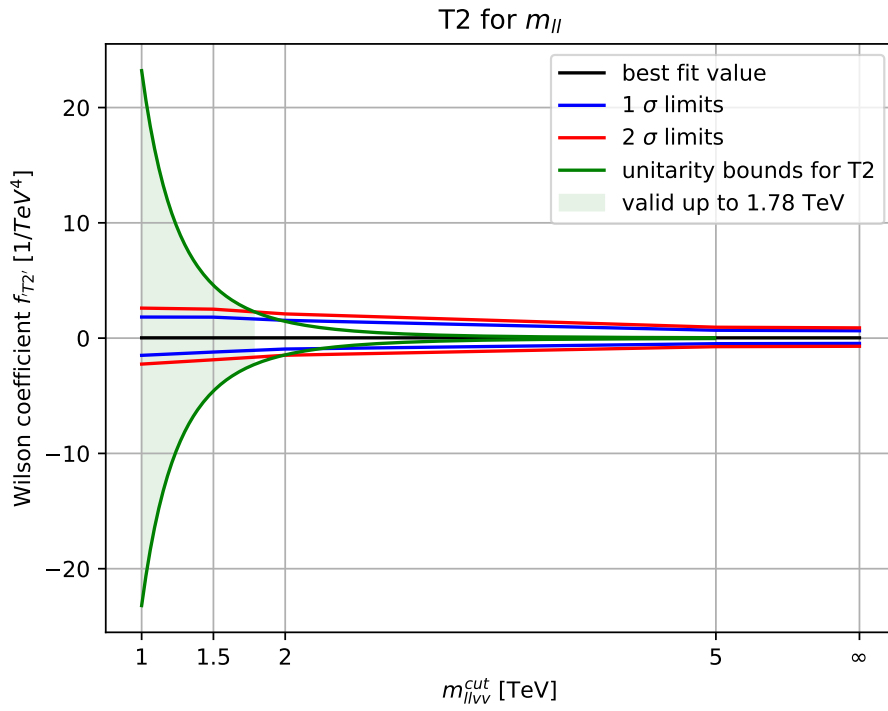
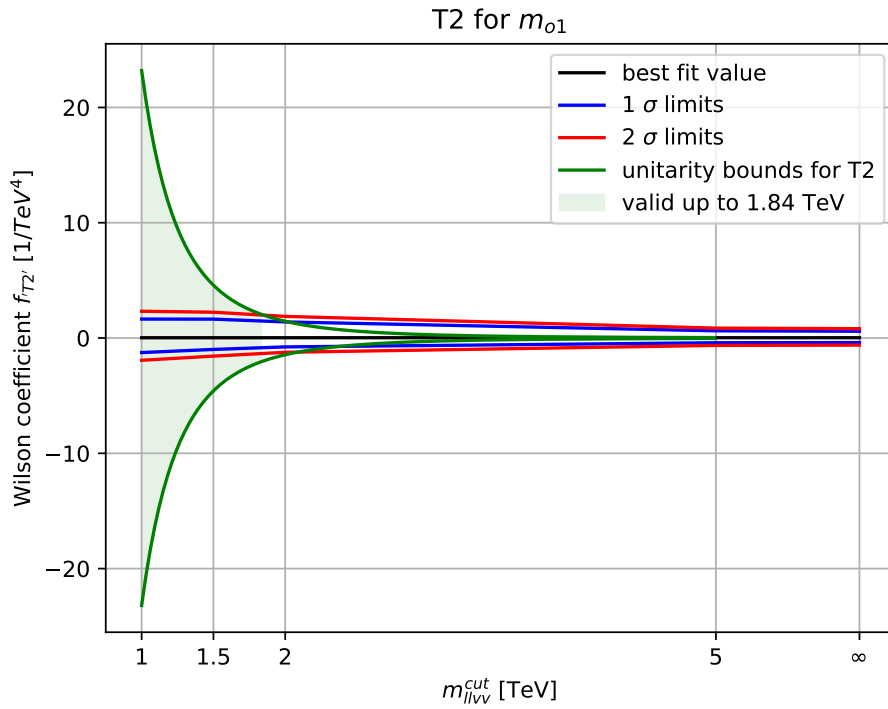
(b) Clipping scan for m_{o1} .(c) Clipping scan for m_T .

Figure 9.7: Limit depiction of Maximum Likelihood fits for T1 in comparison to unitarity bounds. The green area marks the validity range for this operator concerning unitarity.

(a) Clipping scan for m_{II} .(b) Clipping scan for m_{o1} .

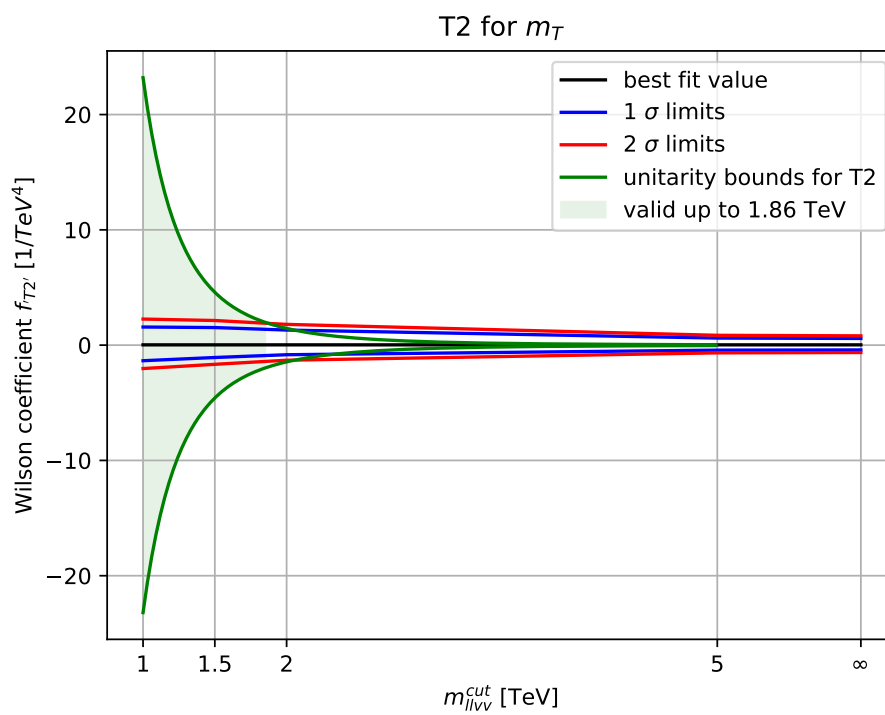
(c) Clipping scan for m_T .

Figure 9.8: Limit depiction of Maximum Likelihood fits for T2 in comparison to unitarity bounds. The green area marks the validity range for this operator concerning unitarity.